



# New method for the preparation of hierarchical nanotube $K_{0.3x}Mn_xCe_{1-x}O_8$ catalysts and their excellent catalytic performance for soot combustion

Chunlei Zhang<sup>a</sup>, Siyu Gao<sup>a</sup>, Shengran Zhou<sup>a</sup>, Di Yu<sup>b</sup>, Lanyi Wang<sup>a</sup>, Xiaoqiang Fan<sup>a</sup>,  
Xuehua Yu<sup>a,\*</sup>, Bing Liu<sup>c,\*</sup>, Zhen Zhao<sup>a,b,\*\*</sup>

<sup>a</sup> Institute of Catalysis for Energy and Environment, College of Chemistry and Chemical Engineering, Shenyang Normal University, Shenyang, Liaoning 110034, China

<sup>b</sup> State Key Laboratory of Heavy Oil Processing, China University of Petroleum, 18# Fuxue Road, Chang Ping, Beijing 102249, China

<sup>c</sup> Department of Chemical Engineering, School of Chemical and Material Engineering, Jiangnan University, Wuxi 214122, China

## ARTICLE INFO

### Keywords:

Soot combustion  
Catalytic removal  
Centrifugal spinning  
Hierarchical nanotube

## ABSTRACT

A series of nanofibrous K-Mn-Ce composite oxide catalysts were prepared via a centrifugal spinning method for the first time, and their physicochemical properties were studied. The prepared  $K_{0.3x}Mn_xCe_{1-x}O_8$  metal oxide catalyst, which is a composite of  $CeO_2$  and cryptopotassium manganese-type  $K_{2-x}Mn_8O_{16}$ , exhibits a hierarchical nanotube structure with uniform nanoneedles on its surface. During the process of soot oxidation,  $CeO_2$  utilizes its unique oxygen storage and release capacity to supply oxygen species. Simultaneously, the excellent redox properties of  $K_{2-x}Mn_8O_{16}$  effectively promote valence cycling of the active components and produce more active oxygen species. This synergistic effect effectively enhances the intrinsic activity of the catalysts. Among the prepared catalysts,  $K_{0.15}Mn_{0.5}Ce_{0.5}O_8$  exhibits the highest catalytic performance, with 10% ( $T_{10}$ ), 50% ( $T_{50}$ ), and 90% ( $T_{90}$ ) soot conversion temperatures of 267 °C, 309 °C, and 338 °C, respectively, and shows good stability and water and sulfur resistance. Based on their simple preparation, low cost, and good catalytic performance,  $K_{0.3x}Mn_xCe_{1-x}O_8$  composite metal oxide catalysts have good potential in catalytic soot combustion applications.

## 1. Introduction

Over the past few decades, diesel engines have played a key role in the development of industries, agriculture, transportation, and other fields due to their advantages such as low cost, high thermal efficiency, and long life. However, the soot particles released from diesel engine exhaust have seriously harmed the environment and pose a threat to the health of humans and other organisms, which has attracted widespread research attention [1,2–3]. To date, catalytic purification technology that combines a diesel particle filter with a soot combustion catalyst is the most promising method for soot removal in post-processing technology, and the development of stable, low-cost and efficient catalysts has become the key factor in soot particle removal [4,5].

The catalytic combustion of soot particles is a kind of multiphase catalytic reaction with deep oxidation. Due to the catalytic combustion reaction of soot has the three-phase catalytic characteristics of gas-solid-(soot)-solid (catalysts), the performance of the catalysts is affected by

both the intrinsic activity and the contact efficiency with soot [6,7]. Previous studies have shown that manganese-based oxide catalysts exhibit strong redox ability based on their valence variability and diversity [8–10]. In addition, the cerium-based oxide catalysts have also attracted the attention of researchers due to their unique oxygen storage and release capacity [11–13]. The manganese-cerium oxide catalysts exhibit excellent intrinsic activity because of the synergistic effect between the active components of manganese and cerium, as well as the modulation among electrons [14–16]. In addition, due to the alkalinity and electron donating ability, alkali metals have been used as catalyst modifiers in previous studies. Meanwhile, alkali metals exhibit the strong ability to improve the contact efficiency between catalysts and soot under the molten state [17,18]. Therefore, the catalytic performance of manganese cerium oxide catalysts can often be further improved under the modification of alkali metals [19,20]. In addition, researchers are also committed to developing special morphologies of catalysts to enhance the contact efficiency between catalysts and soot,

\* Corresponding authors.

\*\* Corresponding author at: Institute of Catalysis for Energy and Environment, College of Chemistry and Chemical Engineering, Shenyang Normal University, Shenyang, Liaoning 110034, China.

E-mail addresses: [yuxuehua1986@163.com](mailto:yuxuehua1986@163.com) (X. Yu), [liubing@jiangnan.edu.cn](mailto:liubing@jiangnan.edu.cn) (B. Liu), [zhaozhen1586@163.com](mailto:zhaozhen1586@163.com), [zhenzhao@cup.edu.cn](mailto:zhenzhao@cup.edu.cn) (Z. Zhao).

<https://doi.org/10.1016/j.apcatb.2024.124169>

Received 25 December 2023; Received in revised form 31 March 2024; Accepted 6 May 2024

Available online 9 May 2024

0926-3373/© 2024 Elsevier B.V. All rights are reserved, including those for text and data mining, AI training, and similar technologies.

such as materials with three-dimensional ordered macropores [21,22], disordered macropores [23,24], nanoparticles [25,26], and nanofibers [27,28]. Among them, the nanofiber catalyst has better capture ability for soot particles due to its high specific surface area and high porosity [29–31].

Currently, the production of nanofiber metal oxide catalysts mainly involves methods, such as electrospinning [32,33], hydrothermal [34,35], and template [36,37] methods. However, due to their disadvantages of low preparation efficiency, high cost, and the requirement for complex equipment, these methods cannot be used to achieve the large-scale preparation of catalysts [38–40]. Here, a centrifugal spinning method, which uses centrifugal force to spin a material at 20 °C, 101 kPa, was applied to synthesize nanofiber metal oxide catalysts. This method has the advantages of being a simple preparation process, having strong practicality, high efficiency, low in cost, and can be easily used to achieve large-scale production [41–43]. Based on the above ideas, a sol-gel method combined with centrifugal spinning technology was used to prepare nanofiber potassium-manganese-cerium composite oxide ( $K_{0.3x}Mn_xCe_{1-x}O_8$ ) catalysts for the first time. Interestingly, a standard commercial cotton candy machine was used as a centrifuge. The physical and chemical properties of the catalysts were characterized using X-ray diffractometry (XRD), scanning electron microscopy (SEM), transmission electron microscopy (TEM),  $N_2$  adsorption-desorption measurements, X-ray photoelectron spectroscopy (XPS), hydrogen temperature-programmed desorption ( $H_2$ -TPR) measurements, and other characterization methods. The activity, stability, and water and sulfur resistance of the catalysts were then evaluated for soot combustion. Based on the characterization and density functional theory (DFT) results, the synergistic effects of the catalyst structure and components on the catalytic performance and mechanisms were also proposed.

## 2. Experimental section

### 2.1. Catalyst preparation

Fibrous K-Mn-Ce composite oxide catalysts ( $K_{0.3x}Mn_xCe_{1-x}O_8$ ) with different ratios of manganese and cerium were prepared via centrifugal spinning using a standard commercial cotton candy machine as a centrifugal device. The detailed synthesis steps are as follows. Potassium acetate, manganese acetate tetrahydrate, and cerium nitrate hexahydrate in different molar ratios were dissolved in a mixed solution of ethanol and water, as shown in Table S1. After obtaining a homogeneous transparent solution, a certain amount of polyvinylpyrrolidone (PVP,  $K_w = 1300000$ ) was dissolved in the above solution, and the mixture was magnetically stirred for 30 min in a water bath (50 °C) to obtain a homogeneous colloidal precursor. After ultrasonication for 10 min, the

precursor was transferred to a commercial cotton candy machine by syringe. The speed of the cotton candy machine was adjusted to 6000 rpm at room temperature. The precursor sol in the syringe was slowly pushed into the rotating head at a constant speed. Then, the precursor was subjected to centrifugal force to eject the precursor fiber from a small hole on the side of the rotating head and collected with collecting rods at a distance of 13.5 cm from the rotating head. The collected fibers were dried at 80 °C for 12 h and calcined in a tubular furnace under an air atmosphere. The temperature program was set to heat to 300 °C from room temperature at a rate of 2 °C·min<sup>-1</sup>. After calcination for 1 h, the temperature was increased to 550 °C after 20 min, and calcination was conducted at 550 °C for 6 h before reducing the heat to room temperature to obtain the corresponding components of the fibrous metal oxide catalysts. The amounts of raw materials and the preparation process of the catalysts are shown in Table S1 and Fig. 1, respectively. The homogeneous precursor sol was centrifugally spun to form a nanofiber precursor. During the drying and calcination process, the sol underwent phase separation and crystal growth to form the hollow nanotube-like catalysts and nanoneedle structures were uniformly distributed on the surface of the nanotubes.

### 2.2. Physical and chemical characterization

XRD patterns were obtained using a Rigaku Ultima IV X-ray diffractometer with CuK $\alpha$  radiation over a scanning range of 10–90° at a scanning rate of 10°·min<sup>-1</sup>.

The surface morphologies of the catalysts were measured using a Hitachi S4800 SEM. Catalyst samples were gold-sprayed prior to observation. TEM images were collected using a Thermo Talos FEI F200X instrument.

The  $N_2$  adsorption-desorption isotherms and detailed texture properties of the catalysts were measured using a Micromeritics TriStar II: 3020 analyzer.

$H_2$ -TPR curves were obtained by AutoChemi II 2920 chemical adsorption instrument. The catalyst (100 mg) was first treated at 300 °C for 1 h in  $N_2$  atmosphere. After cooling to room temperature, the mixture of 10 vol%  $H_2$ /Ar gas was introduced and heated to 850 °C at a rate of 10 °C·min<sup>-1</sup>. A thermal conductivity detector (TCD) was used to monitor the hydrogen consumption signal during the catalyst reduction process.

$O_2$ -TPD curve was obtained by the same instrument as the  $H_2$ -TPR characterization. The catalyst (100 mg) was first treated at 300 °C for 1 h in  $O_2$  atmosphere. After cooling to room temperature, helium was introduced and heated to 850 °C at a rate of 10 °C·min<sup>-1</sup>. A thermal conductivity detector (TCD) was used to monitor the released  $O_2$  signal.

The Soot-TPR curve was obtained by Agilent 7890B gas

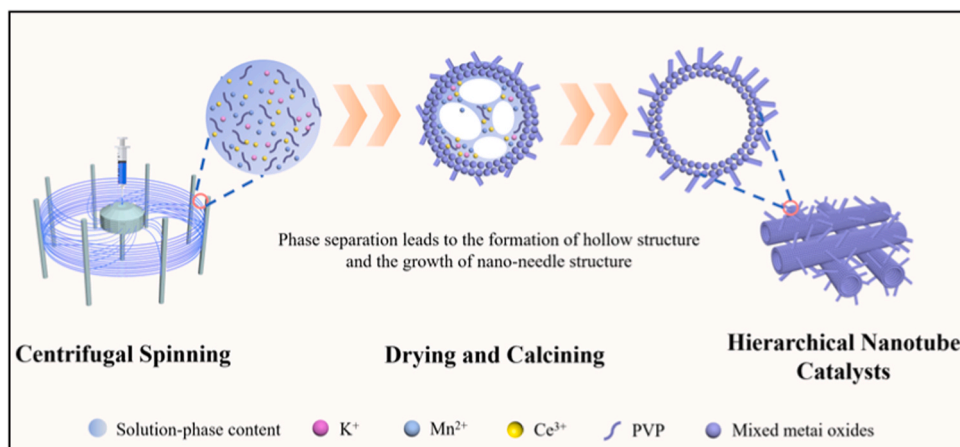


Fig. 1. Schematic diagram of preparation of hierarchical nanotube catalyst by centrifugal spinning.

chromatograph. Argon with a flow rate of 50 ml·min<sup>-1</sup> was introduced into the loose contact soot (10 mg) and catalyst (100 mg), then the temperature was increased from 100 °C to 800 °C at a heating rate of 2 °C·min<sup>-1</sup>.

XPS spectra was obtained by a Thermo ESCALAB 250 Xi instrument. The obtained sample test data are corrected according to the carbon (C 1 s) binding energy of 284.8 eV.

NO-TPO measurements were performed on an FGA10 optical flue gas analyzer. The total flow rate of the reaction gas was 100 ml·min<sup>-1</sup>, the composition of the reaction gas was 800 ppm NO, 10% O<sub>2</sub>, and the balance gas was Ar. The FGA10 optical flue gas analyzer was used to detect NO and NO<sub>2</sub> by non-dispersive ultra-violet (NDUV) method. The principle of optical detection is to use Beer-Lambert Law to calculate the concentration of nitrogen oxides by the intensity of light absorption at different wavelengths.

DRIFTS were characterized on a Vertex 80 v spectrometer (Bruker). The mixture of catalyst and soot with the ratio of 10:1 was pretreated at 300 °C for 30 min under argon protection and then cooled to room temperature. Subsequently, the gas flow was switched to the same gas component as that used to evaluate the catalytic activity, and the spectrum was collected at a heating rate of 5 °C·min<sup>-1</sup> in the temperature range of 50–400 °C in the range of 800–2500 cm<sup>-1</sup>.

Spin-polarized DFT calculations were performed using the Vienna ab initio simulation package (VASP) [44,45]. The model, which developed by Dudarev et al. was used. The Coulomb and exchange interactions were corrected by setting  $U_{\text{eff}} = 3.9$  eV and 5.0 eV ( $U_{\text{eff}}$  is equal to the difference of Coulomb  $U$  minus exchange  $J$ ) for Mn and Ce atoms, respectively [46]. The van der Waals (vdW) interactions were considered in all the DFT calculations by using the D3 correction method (DFT-D3) [47]. The core-valence interactions was represented by projector-augmented wave method [48]. The electron exchange and correlation was simulated by the generalized gradient approximation of Perdew-Burke-Ernzerhof (GGA-PBE) functional [49]. The Gaussian smearing method with the smearing width of 0.05 eV was used. The energy cut off of 520 eV was employed to describe valence electrons on a plane wave basis. During geometric optimization, the force on each ion is minimized by the conjugate gradient algorithm until  $<0.05$  eV/Å, and then the optimized structure is obtained. The value for energy convergence criteria was  $10^{-5}$  eV. The gamma-centered  $1 \times 1 \times 1$  k-point mesh was recognized as surface Brillouin. The transition states (TSs) of elementary reactions were searched by using the climbing-image nudged elastic band (CI-NEB) method developed by Henkelman et al. [50,51]. The calculated TS structure was further verified by analyzing the imaginary frequency. The formation energy of oxygen vacancy ( $E_{\text{Ov}}$ ) was calculated as follows:

$$E_{\text{Ov}} = E_{\text{slab,Ov}} + \frac{1}{2}E_{\text{O}_2} - E_{\text{slab}}$$

where  $E_{\text{slab,Ov}}$  is the energy of the defective slab surface,  $E_{\text{slab}}$  is the energy of the perfect slab surface, and  $E_{\text{O}_2}$  is the energy of the gaseous oxygen molecule.

### 2.3. Activity measurements

The catalytic performance of the catalyst was evaluated by conducting TPO measurements. The soot model was Printx-U particles (diameter 25 nm, purchased from Degussa). A homogeneous mixture of catalyst (100 mg) and soot (10 mg) simulating loose contact was placed in a fixed-bed quartz tube reactor (the diameter of quartz tube is 8 mm). The total flow of the reaction gas was 50 ml·min<sup>-1</sup>, the composition was 2000 ppm NO, 10% O<sub>2</sub>, and Ar was used as the balance gas, and a heating rate 2 °C·min<sup>-1</sup> was employed to heat the reaction from room temperature to the complete burning temperature of the soot. The composition of the outlet gas (mainly nitrogen, nitrogen oxide, carbon dioxide, and carbon monoxide) was analyzed using an on-line gas

chromatograph (GC, Agilent 7890B) and hydrogen flame ionization detector. The  $T_{10}$ ,  $T_{50}$ , and  $T_{90}$  values with conversion rates of the soot particles of 10%, 50%, and 90%, respectively, were used as the basis for evaluating the catalyst activity, and the CO<sub>2</sub> selectivity was calculated using the following equation:

$$S_{\text{CO}_2}^m = \frac{CO_{2\text{out}}^{\text{max}}}{CO_{2\text{out}}^{\text{max}} + CO_{\text{out}}^{\text{max}}} \times 100\%$$

where  $[CO_2]_{\text{out}}^{\text{max}}$  and  $[CO]_{\text{out}}^{\text{max}}$  are the concentrations of CO<sub>2</sub> and CO, respectively, in the reaction products at the temperature ( $T_m$ ) with the fastest burning rate of soot, and  $S_{\text{CO}_2}^m$  is the selectivity of CO<sub>2</sub> at  $T_m$ .

The stability of the catalyst was evaluated by measuring the catalytic performance of the catalyst in five-cycle reactions. In the investigation of the sulfur resistance of the catalysts, the total flow rate of the reaction gas was changed to 50 ml·min<sup>-1</sup>, comprising 2000 ppm NO, 10% O<sub>2</sub>, and different concentrations of SO<sub>2</sub> (10 ppm, 100 ppm, and 300 ppm), with Ar used as the balance gas. To investigate the sulfur and water resistance of the catalysts, the total flow rate of the reaction gas was changed to 50 ml·min<sup>-1</sup>, comprising 2000 ppm NO, 10% O<sub>2</sub>, 10% H<sub>2</sub>O steam, and different concentrations of SO<sub>2</sub> (10 ppm, 100 ppm, and 300 ppm), with Ar used as the balance gas. In addition, in order to investigate the influence of water on the catalysts, the catalysts were treated as follows: soak in water for 12 h, heat treatment in water vapor at 100 °C and 500 °C for 12 h, and then the catalytic activities of the treated catalysts were evaluated by the same way as catalytic activity test. The turnover frequency (TOF) values of the catalysts were determined by a homogeneous mixture of loosely-contacted catalyst and soot in an isothermal combustion reaction at 257 °C. The Agilent 7890B was used to monitor the change of CO<sub>2</sub> concentration before and after the cessation of O<sub>2</sub> flow in the reaction gas.

## 3. Results and discussion

### 3.1. Structural features of the as-prepared catalysts

#### 3.1.1. XRD Patterns of the As-prepared catalysts

XRD diffraction patterns of the prepared catalysts are shown in

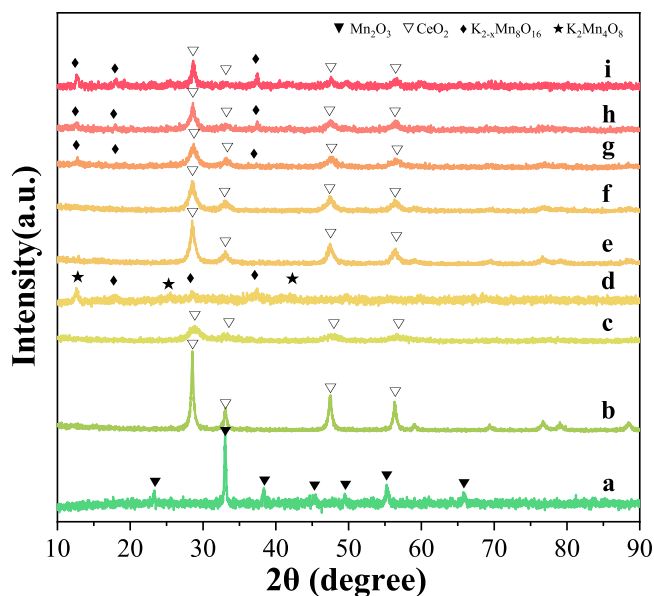


Fig. 2. X-ray diffraction patterns of prepared catalysts. (a): MnO<sub>8</sub>; (b): CeO<sub>2</sub>; (c): MnCeO<sub>8</sub>; (d): K<sub>0.3</sub>MnO<sub>8</sub>; (e): K<sub>0.03</sub>Mn<sub>0.1</sub>Ce<sub>0.9</sub>O<sub>8</sub>; (f): K<sub>0.09</sub>Mn<sub>0.3</sub>Ce<sub>0.7</sub>O<sub>8</sub>; (g): K<sub>0.15</sub>Mn<sub>0.5</sub>Ce<sub>0.5</sub>O<sub>8</sub>; (h): K<sub>0.21</sub>Mn<sub>0.7</sub>Ce<sub>0.3</sub>O<sub>8</sub>; (i): K<sub>0.27</sub>Mn<sub>0.9</sub>Ce<sub>0.1</sub>O<sub>8</sub>; ▼ Mn<sub>2</sub>O<sub>3</sub>, △ CeO<sub>2</sub>, ◆ K<sub>2-x</sub>Mn<sub>8</sub>O<sub>16</sub>, ★ K<sub>2</sub>Mn<sub>4</sub>O<sub>8</sub>.

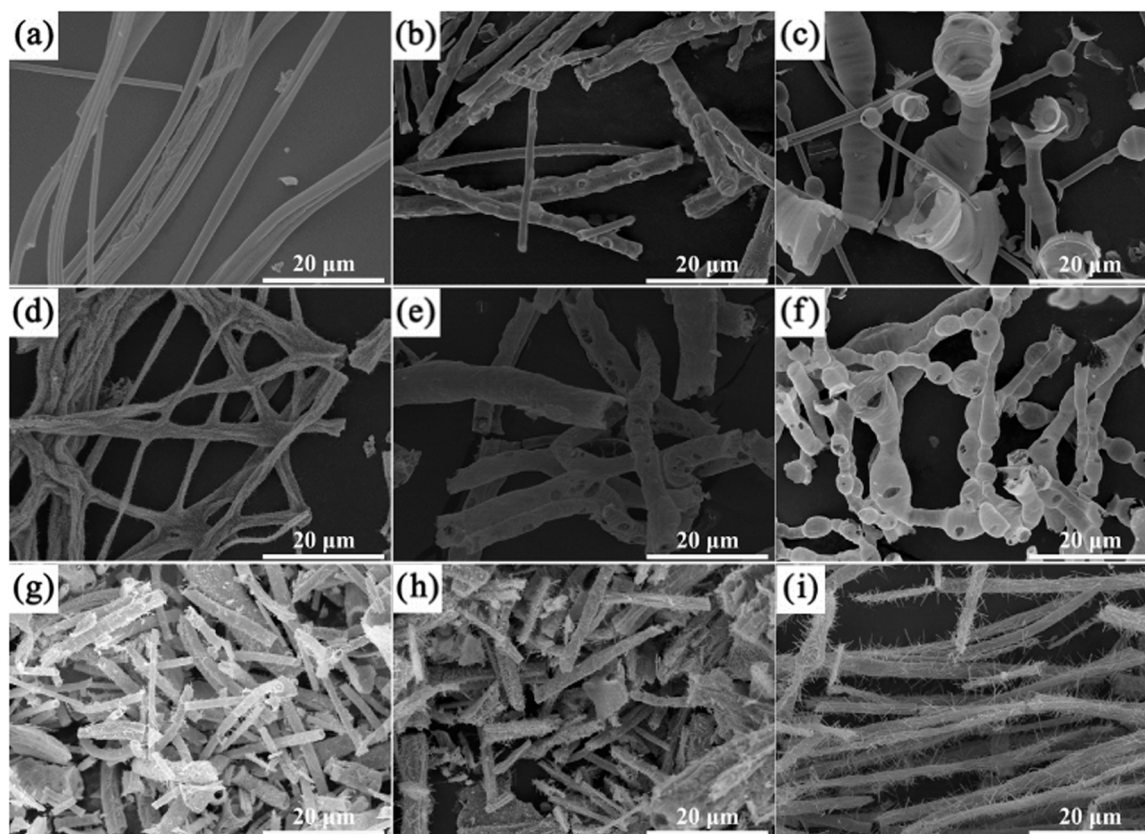


**Fig. 2.** The diffraction peaks of the  $\text{MnO}_8$  catalysts are located at  $2\theta = 23.3^\circ, 33.0^\circ, 38.4^\circ, 45.2^\circ, 49.4^\circ, 55.2^\circ$ , and  $65.8^\circ$ , which are highly consistent with the characteristic peaks of a  $\text{Mn}_2\text{O}_3$  phase (marked as “▼”, JCPDS card No. 41–1442) [52]. The diffraction peaks of the  $\text{CeO}_2$  catalyst are located at  $2\theta = 28.5^\circ, 33.0^\circ, 47.5^\circ$ , and  $56.3^\circ$ , which can be assigned to a  $\text{CeO}_2$  phase (marked as “▽”, JCPDS card No. 34–0294). The diffraction peaks of the  $\text{MnCeO}_8$  catalyst are located at  $2\theta = 28.5^\circ, 33.0^\circ, 47.5^\circ$ , and  $56.3^\circ$ , attributed to the characteristic peaks of crystalline  $\text{CeO}_2$  (marked as “▽”) [53]. However, no characteristic diffraction peaks related to Mn species were observed in the patterns, which can be attributed to the large lattice spacing of  $\text{CeO}_2$ , where Mn species were completely doped into the  $\text{CeO}_2$  lattice. There are two crystal forms of the  $\text{K}_{0.3}\text{MnO}_8$  catalyst, which are cryptomelane  $\text{K}_{2-x}\text{Mn}_8\text{O}_{16}$  (the corresponding diffraction peaks are at  $2\theta = 18.1^\circ, 28.5^\circ$ , and  $37.3^\circ$ , marked as “◆”, JCPDS card No.44–1386) and birnessite  $\text{K}_2\text{Mn}_4\text{O}_8$  (the corresponding diffraction peaks are at  $2\theta = 12.7^\circ, 25.4^\circ$ , and  $42.6^\circ$ , marked as “★”, JCPDS card No.16–0205) [54,55]. The diffraction peaks of the  $\text{K}_{0.03}\text{Mn}_{0.1}\text{Ce}_{0.9}\text{O}_8$  and  $\text{K}_{0.09}\text{Mn}_{0.3}\text{Ce}_{0.7}\text{O}_8$  catalysts are located at  $\theta = 28.6^\circ, 33.1^\circ, 47.5^\circ$ , and  $56.3^\circ$ , which are highly consistent with the characteristic diffraction peaks of a  $\text{CeO}_2$  phase (marked as “▽”). No characteristic peaks related to  $\text{KNO}_3$ ,  $\text{KO}_x$ , or  $\text{MnO}_8$  were observed, which is attributed to a small amount of K and Mn entering the lattice of  $\text{CeO}_2$ . There are two crystal phases in the  $\text{K}_{0.15}\text{Mn}_{0.5}\text{Ce}_{0.5}\text{O}_8$ ,  $\text{K}_{0.21}\text{Mn}_{0.7}\text{Ce}_{0.3}\text{O}_8$ , and  $\text{K}_{0.27}\text{Mn}_{0.9}\text{Ce}_{0.1}\text{O}_8$  catalysts, which are  $\text{CeO}_2$  (the corresponding diffraction peaks are at  $2\theta = 28.6^\circ, 33.1^\circ, 47.5^\circ, 56.3^\circ$ , and  $76.7^\circ$ , marked as “▽”) and cryptomelane  $\text{K}_{2-x}\text{Mn}_8\text{O}_{16}$  (the corresponding diffraction peaks are at  $2\theta = 12.6^\circ, 18.1^\circ$ , and  $37.3^\circ$ , marked as “◆”). On the whole, with an increase in the Mn/Ce ratio, the intensity of the characteristic diffraction peak of  $\text{CeO}_2$  gradually decreases, and the intensity of the characteristic diffraction peak of  $\text{K}_{2-x}\text{Mn}_8\text{O}_{16}$  gradually increases.

### 3.1.2. SEM and TEM images of the as-prepared catalysts

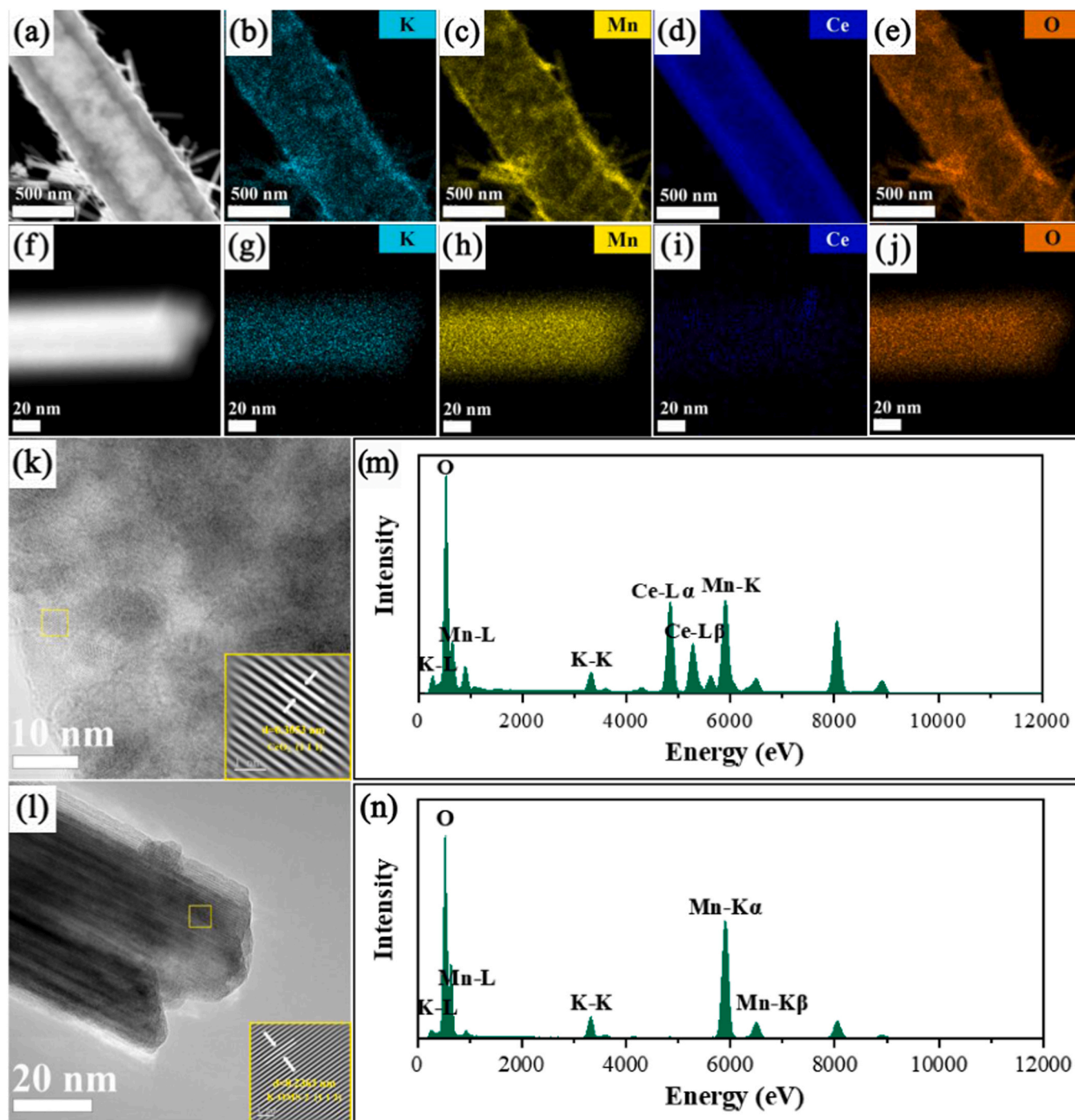
SEM images of the as-prepared catalysts are shown in Fig. 3. It can be observed from the images that all the catalysts exhibit a nanofiber morphology, but the specific configurations of the nanofibers are significantly affected by the catalyst composition. As shown in Fig. 3a, the  $\text{MnO}_8$  catalyst fibers have a uniform diameter and smooth surface; the surfaces of the  $\text{CeO}_2$  and  $\text{K}_{0.03}\text{Mn}_{0.1}\text{Ce}_{0.9}\text{O}_8$  catalyst fibers have a porous structure (Figs. 3b and 3e); the  $\text{MnCeO}_8$  and  $\text{K}_{0.09}\text{Mn}_{0.3}\text{Ce}_{0.7}\text{O}_8$  catalysts exhibit bead-chain structures (Figs. 3c and 3f); and the  $\text{K}_{0.3}\text{MnO}_8$ ,  $\text{K}_{0.15}\text{Mn}_{0.5}\text{Ce}_{0.5}\text{O}_8$ ,  $\text{K}_{0.21}\text{Mn}_{0.7}\text{Ce}_{0.3}\text{O}_8$  and  $\text{K}_{0.27}\text{Mn}_{0.9}\text{Ce}_{0.1}\text{O}_8$  catalysts exhibit a hollow nanotube-like structure, with nanoneedles uniformly distributed on the surface of the nanotubes (Figs. 3d and 3g–i). The reasons for the above phenomena can be explained as follows. The decomposition of PVP and the formation of metal oxides by some metal salts at high temperature cause phase separation, which generates a concentration gradient, resulting in the Kirkendall effect and the formation of hollow nanotubes. At the same time, the formation of part of the crystal structure leads to the growth of nanoneedles on the surface of the nanotubes.

Fig. 4 shows the TEM, HRTEM, and HAADF-STEM EDS elemental scanning images of the  $\text{K}_{0.15}\text{Mn}_{0.5}\text{Ce}_{0.5}\text{O}_8$  catalyst. As shown in Fig. 4a–j, the main elements, K, Mn, Ce, and O, in the nanofiber of  $\text{K}_{0.15}\text{Mn}_{0.5}\text{Ce}_{0.5}\text{O}_8$  are uniformly distributed in the catalyst, indicating that the main nanofibers of the catalyst are a complex of four elements. The nanoneedles on the surface of the nanofibers only clearly exhibit a uniform distribution of K, Mn, and O, indicating that the nanoneedles on the surface of the catalyst are composed of K, Mn, and O, with little or no Ce. These results are also consistent with the EDS spectra of the  $\text{K}_{0.15}\text{Mn}_{0.5}\text{Ce}_{0.5}\text{O}_8$  catalyst shown in Fig. 4m and n. As shown in Fig. 4k and l, clear lattice stripes with a lattice spacing of 0.305 nm can be observed on the nanotubes and nanoneedles, corresponding to the (111) crystal plane of  $\text{CeO}_2$ ; the lattice spacing on the nanoneedles is



**Fig. 3.** SEM images of prepared catalysts. (a):  $\text{MnO}_8$ ; (b):  $\text{CeO}_2$ ; (c):  $\text{MnCeO}_8$ ; (d):  $\text{K}_{0.3}\text{MnO}_8$ ; (e):  $\text{K}_{0.03}\text{Mn}_{0.1}\text{Ce}_{0.9}\text{O}_8$ ; (f):  $\text{K}_{0.09}\text{Mn}_{0.3}\text{Ce}_{0.7}\text{O}_8$ ; (g):  $\text{K}_{0.15}\text{Mn}_{0.5}\text{Ce}_{0.5}\text{O}_8$ ; (h):  $\text{K}_{0.21}\text{Mn}_{0.7}\text{Ce}_{0.3}\text{O}_8$ ; (i):  $\text{K}_{0.27}\text{Mn}_{0.9}\text{Ce}_{0.1}\text{O}_8$ .





**Fig. 4.** HAADF-STEM images of  $K_{0.15}Mn_{0.5}Ce_{0.5}O_8$  (a,f) and corresponding EDS elemental mapping images (b-e; h-j); HRTEM images of  $K_{0.15}Mn_{0.5}Ce_{0.5}O_8$  (k-l); EDS spectra of  $K_{0.15}Mn_{0.5}Ce_{0.5}O_8$  (m-n).

0.236 nm, corresponding to the (112) crystal plane of K-OMS-2.

### 3.1.3. $N_2$ Adsorption-desorption Isotherms of the As-prepared catalysts

Fig. S1 shows the  $N_2$  adsorption-desorption isotherms and pore size distributions of the as-prepared catalysts. It can be observed from Fig. S1A that all the samples are typical type-IV isotherms, which are the characteristics of mesoporous structure. As shown in Fig. S1A (a, b, d, h, and i), a hysteresis loop was observed in the higher relative pressure range, and no adsorption saturation plateau was observed. The hysteresis loop type was H3 type, indicating that the  $MnO_8$ ,  $CeO_8$ ,  $K_{0.3}MnO_8$ ,  $K_{0.21}Mn_{0.7}Ce_{0.3}O_8$ , and  $K_{0.27}Mn_{0.9}Ce_{0.1}O_8$  catalysts have the slit-like structures resulting from particle accumulation, and the pore

structure was irregular. As shown in Fig. S1A (c, e-g), it is observed that the inclined adsorption and desorption curves form a hysteresis loop, and there is a saturated adsorption plateau in the isotherm. The hysteresis loop type is H1 type, reflecting a uniform pore size distribution and the mesoporous pore size distribution is relatively narrow, which is consistent with the data shown in Fig. S1B (c, e-g). Detailed data on the texture properties of the prepared samples are listed in Table S2. The specific surface area of the  $K_{0.03x}Mn_xCe_{1-x}O_8$  catalysts varies in the range of 16.9–51.4  $m^2/g$ . With an increase in the manganese-cerium ratio, the specific surface area and pore size of the catalysts show an increasing trend.

### 3.1.4. $H_2$ -TPR and $O_2$ -TPD results of the As-prepared catalysts

The catalytic oxidation of soot particles is a gas-solid-solid deep oxidation reaction. The redox performance of catalysts has a significant impact on their activity. Therefore, it is of great significance to study the reduction ability of the catalyst by TPD. The reduction peaks of this series of catalysts can be divided into two categories, as shown in Fig. 5A. The reduction peak below 400 °C is attributed to the reduction of Mn species, which can be divided into three peaks. As shown in the  $H_2$ -TPR results, the three reduction peaks are attributed to the reduction of surface chemisorbed oxygen, the reduction of  $Mn^{4+}$  to  $Mn^{3+}$ , and the reduction of  $Mn^{3+}$  to  $Mn^{2+}$  from low temperature to 400 °C [56]. The reduction peaks above 400 °C are related to the reduction of  $CeO_2$ . When Ce is relatively high in the  $CeO_8$ ,  $MnCeO_8$ ,  $K_{0.03}Mn_{0.1}Ce_{0.9}O_8$ , and  $K_{0.09}Mn_{0.3}Ce_{0.7}O_8$  catalysts, a weak reduction peak appears in the range of 400–600 °C, which can be assigned to the reduction of surface  $CeO_2$  to

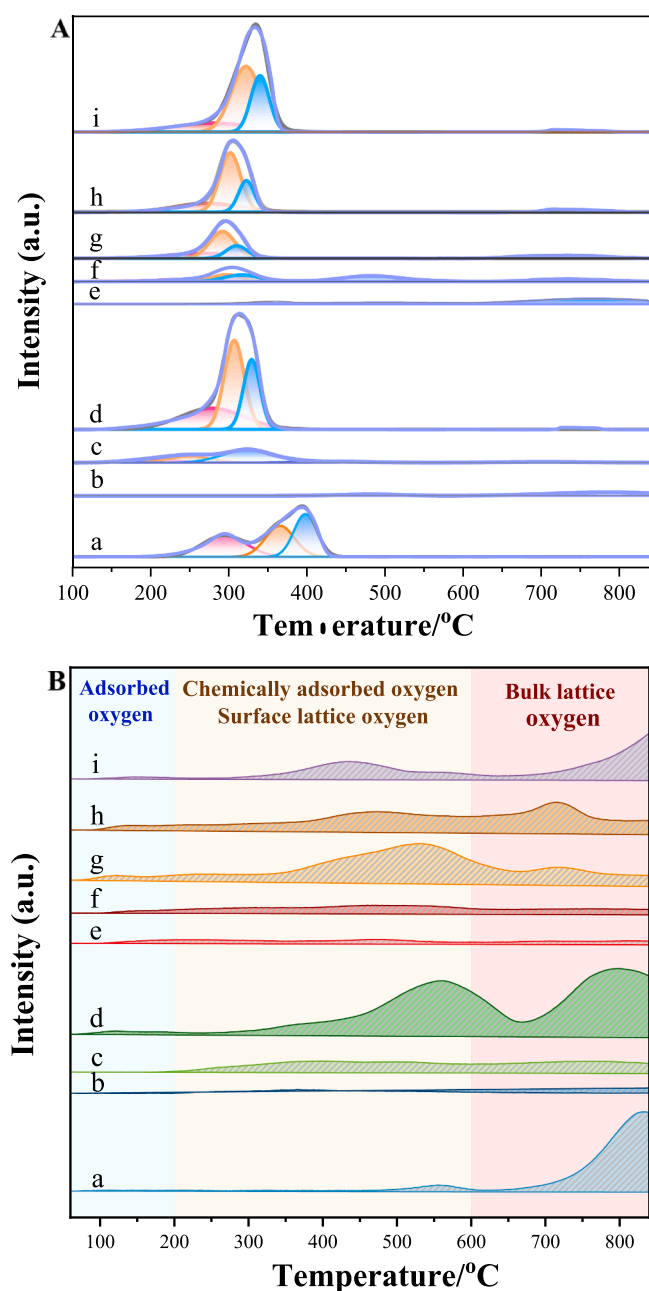


Fig. 5.  $H_2$ -TPR (A) and  $O_2$ -TPD (B) curves of as prepared catalysts. (a):  $MnO_8$ ; b:  $CeO_8$ ; c:  $MnCeO_8$ ; d:  $K_{0.3}MnO_8$ ; e:  $K_{0.03}Mn_{0.1}Ce_{0.9}O_8$ ; f:  $K_{0.09}Mn_{0.3}Ce_{0.7}O_8$ ; g:  $K_{0.15}Mn_{0.5}Ce_{0.5}O_8$ ; h:  $K_{0.21}Mn_{0.7}Ce_{0.3}O_8$ ; i:  $K_{0.27}Mn_{0.9}Ce_{0.1}O_8$ ).

$Ce_2O_3$  [57]. In general, the reducibility of the catalyst is closely related to the temperature and peak area of the reduction peak. The lower the reduction peak temperature, the easier it is to reduce the sample. The larger the reduction peak area, the more hydrogen is consumed. In the  $K_{0.3}Mn_xCe_{1-x}O_8$  catalysts, combined with the XRD results, it can be seen that the change of Mn/Ce ratio will lead to the change of the proportion of  $K_{2-x}Mn_8O_{16}$  and  $CeO_2$  phases. With an increase in the Mn/Ce ratio, the peak area of the reduction peak mainly related to Mn below 400 °C increased significantly, while the peak area mainly related to Ce above 400 °C decreased significantly. In this study, all the catalysts can process soot particles below 400 °C. Therefore, the reduction peak below 400 °C is of great significance for catalytic soot combustion. In addition, the temperature of the reduction peak below 400 °C shows an overall trend of first shifting toward a low temperature and then toward the high-temperature region in line with an increase in the manganese-cerium ratio. Among the catalysts,  $K_{0.15}Mn_{0.5}Ce_{0.5}O_8$  exhibits the lowest reduction peak temperature.

Active oxygen species are an important class of oxides in soot catalytic combustion. Therefore, the as-prepared catalysts were characterized by conducting  $O_2$ -TPD measurements. From Fig. 5B, we can see that the desorption curves can be divided into three regions. The first region (50–200 °C) corresponds to the desorption of physically-adsorbed and weak chemically-adsorbed surface oxygen; the second region (200–600 °C) can be assigned to the desorption of strongly chemisorbed oxygen species and surface lattice oxygen; and the third region (>600 °C) corresponds to the desorption of bulk lattice oxygen [58]. As the temperature for the complete combustion of soot particles is <400 °C, the active oxygen species in the first and second regions are of great significance for improving catalytic activity. From Fig. 5B, it can be observed that compared to other catalysts, the  $K_{0.3}MnO_8$ ,  $K_{0.15}Mn_{0.5}Ce_{0.5}O_8$ ,  $K_{0.21}Mn_{0.7}Ce_{0.3}O_8$ , and  $K_{0.27}Mn_{0.9}Ce_{0.1}O_8$  catalysts exhibit the desorption of more oxygen species in the first and second temperature regions, and, therefore, it can be speculated that these catalysts contain more oxygen vacancies. In particular, the  $K_{0.15}Mn_{0.5}Ce_{0.5}O_8$  catalyst exhibits the highest desorption of most low-temperature oxygen species at <400 °C, inferring that more reaction oxygen species can be involved in the catalytic reaction in the process of catalytic soot combustion.

### 3.1.5. Soot-TPR curves of the As-prepared catalysts

Fig. 6 shows the TPR curves of five representative catalysts ( $MnO_8$ ,

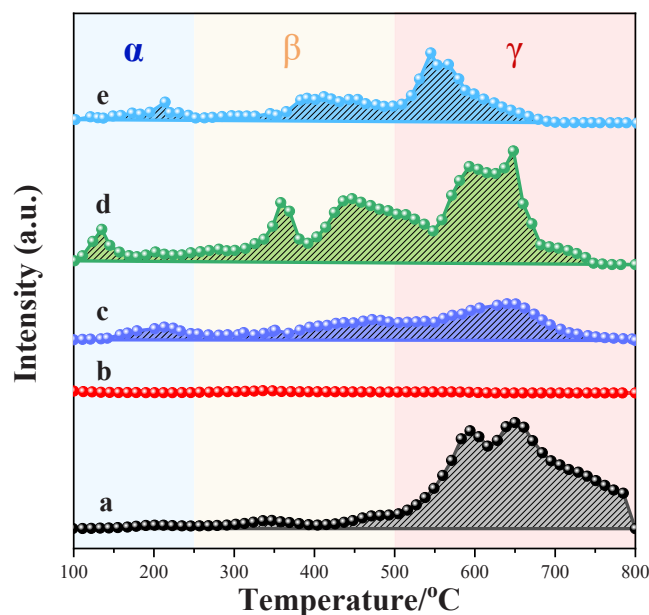


Fig. 6. Soot-TPR curves of as prepared catalysts. (a):  $MnO_8$ ; b:  $CeO_8$ ; c:  $MnCeO_8$ ; d:  $K_{0.3}MnO_8$ ; e:  $K_{0.15}Mn_{0.5}Ce_{0.5}O_8$ ).

CeO<sub>8</sub>, Mn<sub>0.5</sub>Ce<sub>0.5</sub>O<sub>8</sub>, K<sub>0.3</sub>MnO<sub>8</sub>, and K<sub>0.15</sub>Mn<sub>0.5</sub>Ce<sub>0.5</sub>O<sub>8</sub>) with soot as a reducing agent under argon atmosphere. In the process of temperature rise reduction, soot can only be oxidized by surface adsorption, sub-surface adsorption, and lattice oxygen species present on the catalyst, accompanied by the reduction process of metal ions. These oxygen species are desorbed without gaseous oxygen supplementation to ensure cyclic oxidation. From Fig. 6, it can be observed that the soot oxidation process can be roughly divided into three temperature ranges, α (100–250 °C), β (250–500 °C) and γ (500–800 °C), corresponding to the consumption of surface adsorbed oxygen, subsurface adsorbed oxygen and bulk oxygen, respectively, which is consistent with the characterization results of O<sub>2</sub>-TPD [59]. According to the temperature range of soot oxidation elimination (200–400 °C), surface-adsorbed oxygen and subsurface-adsorbed oxygen species are the main reaction oxygen species involved in soot oxidation. As shown in Figs. 6d and 6e, the K<sub>0.3</sub>MnO<sub>8</sub> and K<sub>0.15</sub>Mn<sub>0.5</sub>Ce<sub>0.5</sub>O<sub>8</sub> catalysts contain the most reaction oxygen species in this temperature range.

### 3.1.6. XPS spectra of the As-prepared catalysts

In addition to the inherent redox properties, the surface compositions and oxidation states of the elements in the catalyst are also significant factors that affect catalytic performance. Five representative catalysts (MnO<sub>8</sub>, CeO<sub>8</sub>, Mn<sub>0.5</sub>Ce<sub>0.5</sub>O<sub>8</sub>, K<sub>0.3</sub>MnO<sub>8</sub>, and K<sub>0.15</sub>Mn<sub>0.5</sub>Ce<sub>0.5</sub>O<sub>8</sub>) were characterized by XPS, the results are shown in Table 1 and Fig. 7. As presented in Fig. 7A, the Mn 2p spectrum is relatively wide, and there is a certain degree of asymmetry in the two Mn 2p<sub>3/2</sub> and Mn 2p<sub>1/2</sub> peaks. Due to the partial overlap of the XPS peaks of Mn<sup>2+</sup>, Mn<sup>3+</sup>, and Mn<sup>4+</sup>, it is difficult to determine the oxidation state of manganese solely based on the Mn 2p spectra. However, the splitting amplitude of Mn 3s decreases with an increase in the average oxidation state of manganese, which was used to verify the oxidation state of manganese. The Mn 3s multiplet splitting energy (ΔE) is associated with the average valence state of manganese as follows: average valence state = 8.95–1.13 × ΔE [60]. As shown in Fig. 7B, the ΔE values of the MnO<sub>8</sub>, Mn<sub>0.5</sub>Ce<sub>0.5</sub>O<sub>8</sub>, K<sub>0.3</sub>MnO<sub>8</sub>, and K<sub>0.15</sub>Mn<sub>0.5</sub>Ce<sub>0.5</sub>O<sub>8</sub> catalysts are 5.56 eV, 5.36 eV, 4.78 eV, and 4.78 eV, respectively. Therefore, the average valence states of Mn in the MnO<sub>8</sub>, Mn<sub>0.5</sub>Ce<sub>0.5</sub>O<sub>8</sub>, K<sub>0.3</sub>MnO<sub>8</sub>, and K<sub>0.15</sub>Mn<sub>0.5</sub>Ce<sub>0.5</sub>O<sub>8</sub> catalysts are 2.67, 2.89, 3.55, and 3.55, respectively. The average Mn valence state of the K<sub>0.3</sub>MnO<sub>8</sub> and K<sub>0.15</sub>Mn<sub>0.5</sub>Ce<sub>0.5</sub>O<sub>8</sub> catalysts is significantly higher than that of the other catalysts, which is consistent with other XPS measurements. Moreover, the Mn<sup>4+</sup> abundance of the K<sub>0.3</sub>MnO<sub>8</sub> (54.87%) and K<sub>0.15</sub>Mn<sub>0.5</sub>Ce<sub>0.5</sub>O<sub>8</sub> (54.88%) catalysts is higher than that of the other catalysts, as listed in Table 1.

The Ce 3d spectra of the catalysts are shown in Fig. 7C. The XPS of Ce 3d can be fitted to eight peaks, corresponding to four pairs of spin-orbit bistates. The peaks marked as (α'', α', α) and (β'', β', β) can be attributed to Ce<sup>4+</sup> 3d<sub>3/2</sub> and Ce<sup>4+</sup> 3d<sub>5/2</sub>, and the peaks marked as (α', α'') and (β', β'') can be attributed to Ce<sup>3+</sup> 3d<sub>3/2</sub> and Ce<sup>3+</sup> 3d<sub>5/2</sub> [61], respectively. The α'', α', α, β'', β', and β peaks for Ce<sup>4+</sup> are much stronger than those of α' and β' for Ce<sup>3+</sup>, indicating that Ce<sup>4+</sup> is the main valence state of the catalysts. As shown in Table 1, the Ce<sup>4+</sup> species content (87.83%) of the CeO<sub>8</sub> catalyst is the highest. After K and Mn doping, the Ce<sup>4+</sup> species content in the Mn<sub>0.5</sub>Ce<sub>0.5</sub>O<sub>8</sub> and K<sub>0.15</sub>Mn<sub>0.5</sub>Ce<sub>0.5</sub>O<sub>8</sub> catalysts decreased, and the Ce<sup>3+</sup> species content increased. To maintain charge balance, an increase in

Ce<sup>3+</sup> species is beneficial to the formation of oxygen vacancies, and more active oxygen species are produced, which is conducive to the catalytic combustion of soot.

As shown in Fig. 7D, O 1s can be fitted into three types of O species, namely O-I, O-II and O-III. The O-I species located at binding energy of 532.39–533.10 eV are attributed to surface adsorbed oxygen species or surface H<sub>2</sub>O/OH. The O-II species located at binding energy of 531.07–531.78 eV can be attributed to partially chemisorbed oxygen or low-coordinated defective oxides. The O-III species located at binding energy of 529.35–529.82 eV can be attributed to lattice oxygen ions bonded to metal cations [62]. As shown in Table 1, the K<sub>0.03</sub>Mn<sub>0.1</sub>Ce<sub>0.9</sub>O<sub>8</sub> catalysts contain a higher abundance of O-II species, which is highly consistent with the O<sub>2</sub>-TPD characterization results.

### 3.1.7. NO-TPO results of the prepared catalysts

NO<sub>2</sub> with strong oxidation is an important species of indirect oxidation of soot during catalytic soot combustion, the nitrogen oxides conversion ability of the catalysts will also significantly affect their activity. Fig. 8 shows the conversion curves of the NO<sub>x</sub> and CO<sub>2</sub> of the prepared catalyst with temperature. As shown in Figs. 8A and 8C, both the MnO<sub>8</sub> and MnCeO<sub>8</sub> catalysts exhibit good nitrogen oxide conversion ability, and the peak temperature of NO<sub>2</sub> formed by conversion is around 264 °C. However, due to the peak concentration of NO<sub>2</sub> being reached too early, the temperature window for main soot combustion catalyzed by MnO<sub>8</sub> and MnCeO<sub>8</sub> is missed. From Fig. 8B, it can be observed that the nitrogen oxide conversion ability of the CeO<sub>8</sub> catalyst is poor. As shown in Figs. 8D and 9E, the K<sub>0.3</sub>MnO<sub>8</sub> and K<sub>0.15</sub>Mn<sub>0.5</sub>Ce<sub>0.5</sub>O<sub>8</sub> catalysts also exhibit excellent nitrogen oxide conversion ability. At 219 °C and 196 °C, the NO concentration curve shows an obvious trend of first decreasing and then increasing, indicating that nitrogen oxides are adsorbed on the catalyst surface due to the alkalinity of the alkali metal K and stored as nitrate species at this temperature. The peak concentrations of NO<sub>2</sub> were reached at 324 °C and 297 °C for the K<sub>0.3</sub>MnO<sub>8</sub> and K<sub>0.15</sub>Mn<sub>0.5</sub>Ce<sub>0.5</sub>O<sub>8</sub> catalysts, respectively, which is close to their T<sub>m</sub> values (332 °C and 311 °C), indicating that the NO<sub>2</sub> generated by conversion can participate to a great extent in the catalytic combustion reaction of soot.

## 3.2. Catalytic performance of the as-prepared catalysts

### 3.2.1. Catalytic activities for soot combustion

The catalytic activity of the prepared catalyst for soot combustion is shown in Table 2. The results show that the catalytic activity of single metal oxide catalysts (MnO<sub>8</sub>, CeO<sub>8</sub>) can be significantly improved by potassium doping (K<sub>0.3</sub>MnO<sub>8</sub>) and manganese-cerium composite (MnCeO<sub>8</sub>). Therefore, the hollow-nanotube-structured potassium-doped catalysts with different manganese-cerium ratios (K<sub>0.3x</sub>Mn<sub>x</sub>Ce<sub>1-x</sub>O<sub>8</sub>) showed excellent catalytic performance, significantly reduced the temperature of soot combustion, and exhibited the CO<sub>2</sub> selectivity of >98%. With an increase in the Mn/Ce ratio, the catalytic activity of the catalysts showed a trend of first increasing and then decreasing. Among the catalysts, K<sub>0.15</sub>Mn<sub>0.5</sub>Ce<sub>0.5</sub>O<sub>8</sub> exhibited the best catalytic activity, with T<sub>10</sub>, T<sub>50</sub>, T<sub>90</sub>, and SCo<sub>2</sub><sup>90</sup>/°C values of 267 °C, 309 °C, 338 °C, and 98.9%, respectively. Surprisingly, the catalytic activity of K<sub>0.15</sub>Mn<sub>0.5</sub>Ce<sub>0.5</sub>O<sub>8</sub>

**Table 1**  
Parameters of the fitted components on surface from Mn 2p, Ce 3d and O 1s XPS spectra.

Sample	Mn			Ce		O		
	Molar fraction							
	Mn <sup>4+</sup>	Mn <sup>3+</sup>	Mn <sup>2+</sup>	Ce <sup>4+</sup>	Ce <sup>3+</sup>	O <sub>latt</sub>	O <sub>ads</sub>	O <sub>sur</sub>
MnO <sub>8</sub>	22.21%	22.20%	55.59%	-	-	60.98%	22.40%	16.62%
CeO <sub>8</sub>	-	-	-	87.83%	12.17%	72.27%	14.71%	13.02%
Mn <sub>0.5</sub> Ce <sub>0.5</sub> O <sub>8</sub>	30.19%	28.97%	40.84%	80.34%	19.66%	61.48%	23.97%	14.55%
K <sub>0.3</sub> MnO <sub>8</sub>	54.87%	45.13%	-	-	-	62.00%	24.21%	13.79%
K <sub>0.15</sub> Mn <sub>0.5</sub> Ce <sub>0.5</sub> O <sub>8</sub>	54.88%	45.12%	-	84.62%	15.38%	63.98%	24.58%	11.44%



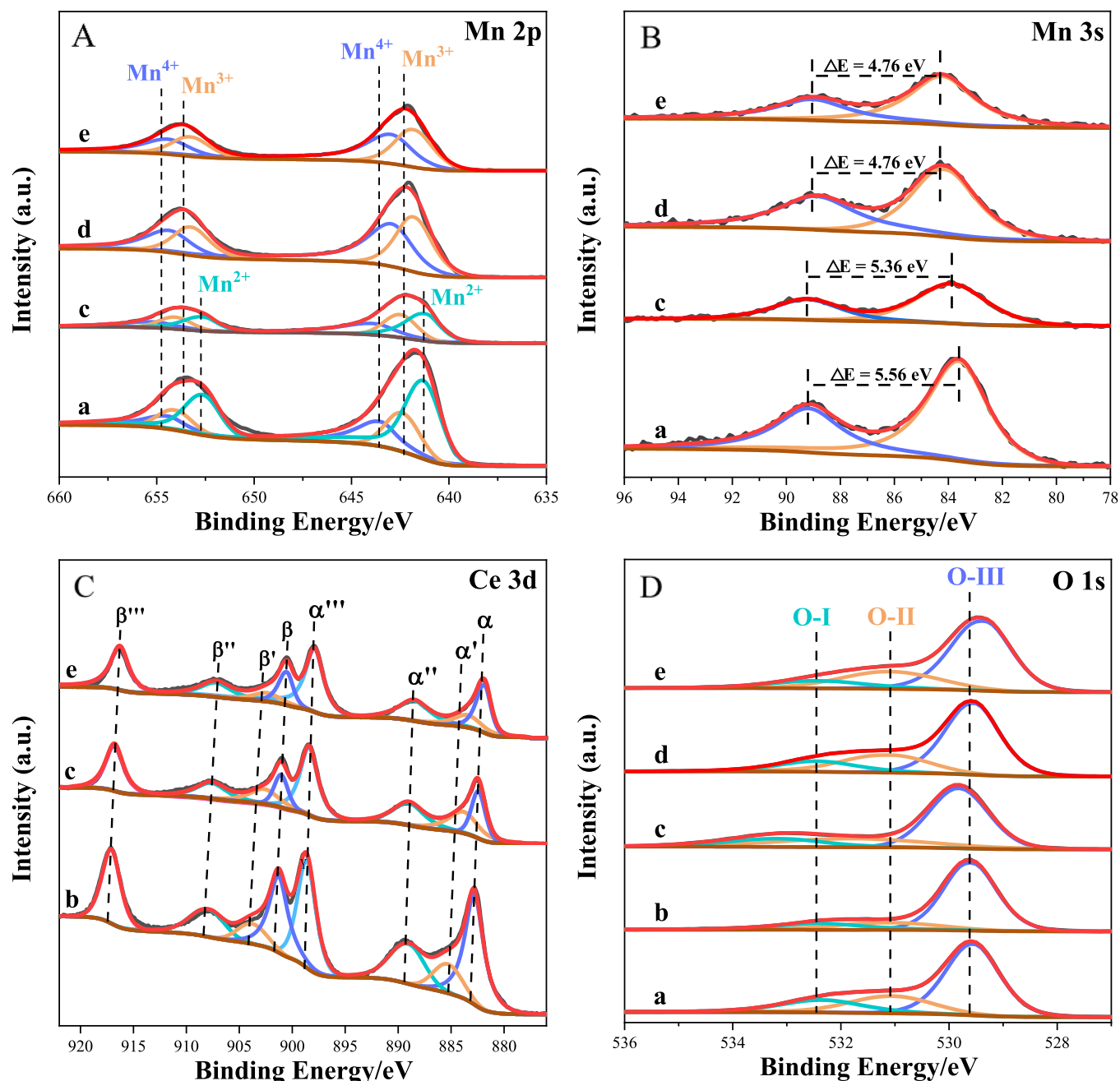


Fig. 7. XPS spectra of Mn 2p (A), Mn 3s (B), Ce 3d (C) and O 1s (D) of as-prepared catalysts. (a:  $\text{MnO}_x$ ; b:  $\text{CeO}_x$ ; c:  $\text{MnCeO}_x$ ; d:  $\text{K}_{0.3}\text{MnO}_x$ ; e:  $\text{K}_{0.15}\text{Mn}_{0.5}\text{Ce}_{0.5}\text{O}_x$ ).

catalyst is comparable to or even higher than that of reported noble metal catalysts. In order to better compare the catalytic performance of the prepared catalysts, the catalytic activities of the catalysts with the active components of K, Mn, and Ce reported in the literature in recent years are summarized in Table 3. Due to the deviations of catalyst dosage, contact conditions, reaction gas and other experimental conditions, it is difficult to finely compare the activities of various catalysts. However, it is still feasible to roughly compare the performance of various catalysts by listed their reaction conditions. As shown in Table 3, the  $T_{10}$ ,  $T_{50}$ , and  $T_{90}$  temperatures of the  $\text{K}_{0.15}\text{Mn}_{0.5}\text{Ce}_{0.5}\text{O}_x$  catalyst are much lower than those of most similar catalysts, showing extremely excellent catalytic performance 63 64 65 66 67 68 69 70 71 72 73 74 75 76 77 78 79. To better explore the intrinsic activity of the catalyst, the change of  $\text{CO}_2$  concentration on the catalyst surface with time was measured under anaerobic conditions at  $257^\circ\text{C}$ . It can be observed from Fig. S3 that the  $\text{K}_{0.15}\text{Mn}_{0.5}\text{Ce}_{0.5}\text{O}_x$  catalyst has the highest amount of

active oxygen species. Generally, the activity of a catalyst can be positively correlated with the amount of active oxygen species it contains. Therefore, it can be concluded that the amount of active oxygen is one of the fundamental factors that affects the performance of a catalyst.

### 3.2.2. Stability of the $\text{K}_{0.15}\text{Mn}_{0.5}\text{Ce}_{0.5}\text{O}_x$ catalyst

The stability of a catalyst is one of its most important properties, especially for practical applications. Therefore, the stability of the  $\text{K}_{0.15}\text{Mn}_{0.5}\text{Ce}_{0.5}\text{O}_x$  catalyst was tested by using it for five reaction cycles. As shown in Fig. 9A, after five cycles of reaction under loose contact, the  $T_{10}$ ,  $T_{50}$ , and  $T_{90}$  values of the  $\text{K}_{0.15}\text{Mn}_{0.5}\text{Ce}_{0.5}\text{O}_x$  catalyst were  $275 \pm 9$ ,  $316 \pm 8$ , and  $345 \pm 7^\circ\text{C}$ , respectively. Moreover, the  $\text{CO}_2$  selectivity values were still  $>98\%$  after five reaction cycles, which also indicates that the catalyst exhibits good stability (Fig. 9B). In addition, to further prove the stability of the  $\text{K}_{0.15}\text{Mn}_{0.5}\text{Ce}_{0.5}\text{O}_x$  catalyst, the used catalyst was characterized by XRD and Raman spectroscopy. The XRD and

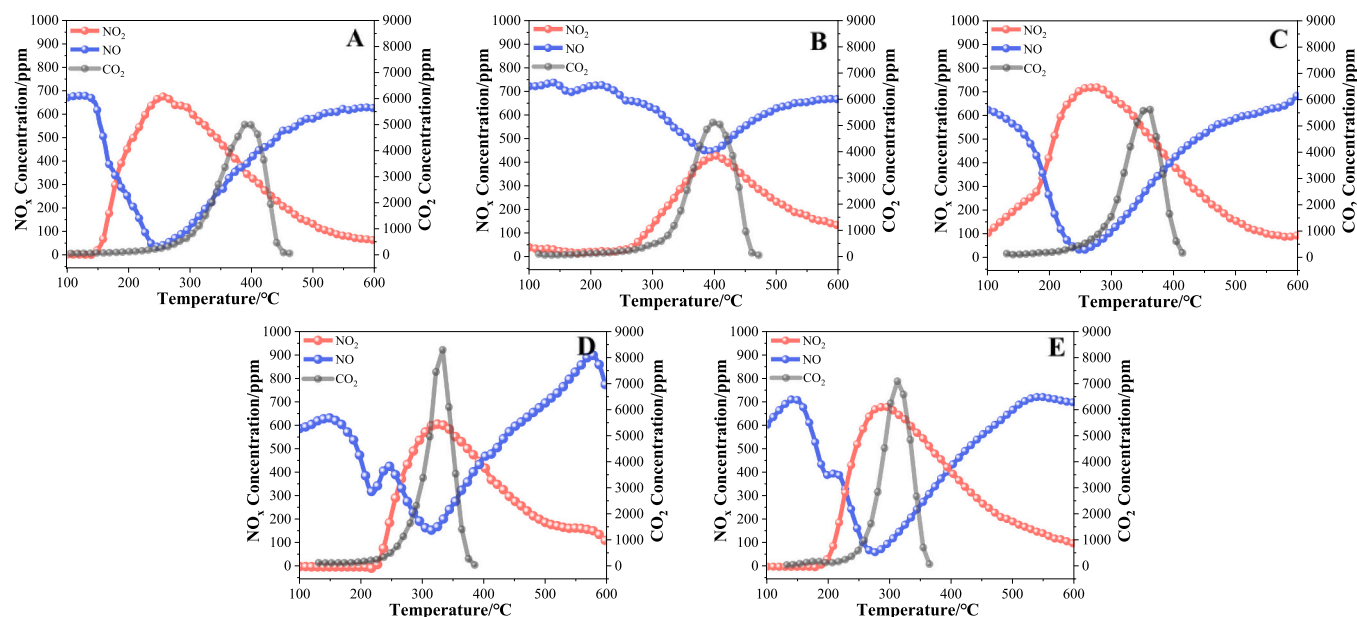


Fig. 8. NO, NO<sub>2</sub> and CO<sub>2</sub> concentration over as prepared catalysts. (A: MnO<sub>x</sub>; B: CeO<sub>x</sub>; C: MnCeO<sub>x</sub>; D: K<sub>0.3</sub>MnO<sub>x</sub>; E: K<sub>0.15</sub>Mn<sub>0.5</sub>Ce<sub>0.5</sub>O<sub>8</sub>).

Raman results of the catalyst were not different from those of the fresh catalyst, indicating that the phase structures of the catalyst were well maintained after soot combustion (Figs. 9C and 9D).

### 3.2.3. Water and sulfur resistance of the K<sub>0.15</sub>Mn<sub>0.5</sub>Ce<sub>0.5</sub>O<sub>8</sub> catalyst

SO<sub>2</sub>, which is present in diesel engine exhaust, usually has a negative impact on soot combustion catalysts. Therefore, it is necessary to study the ability of the catalyst to resist sulfur poisoning. To evaluate the sulfur resistance of the K<sub>0.15</sub>Mn<sub>0.5</sub>Ce<sub>0.5</sub>O<sub>8</sub> catalyst, the effects of different concentrations of SO<sub>2</sub> on the catalytic performance of the catalyst were tested under reaction atmospheres containing 10 ppm, 100 ppm, and 300 ppm SO<sub>2</sub>. As shown in Fig. 9E, the results show that the catalytic performance of the K<sub>0.15</sub>Mn<sub>0.5</sub>Ce<sub>0.5</sub>O<sub>8</sub> catalyst remained basically unchanged under a reaction atmosphere with a low concentration of 10 ppm SO<sub>2</sub>, indicating that the catalyst has certain sulfur resistance. When 100 ppm SO<sub>2</sub> was present in the reaction atmosphere, the catalytic activity of the catalyst decreased slightly. When the SO<sub>2</sub> concentration in the reaction atmosphere increased to 300 ppm, the catalytic activity of the catalyst decreased significantly, especially the T<sub>90</sub> value. In order to further study the reasons for the decrease of the activity of the catalyst in the high concentration SO<sub>2</sub> reaction gas stream, the corresponding Raman spectra of the fresh K<sub>0.15</sub>Mn<sub>0.5</sub>Ce<sub>0.5</sub>O<sub>8</sub> catalyst and the used one under high SO<sub>2</sub> concentration were measured, respectively. As shown in Fig. S4, the significant blue shift of the Raman peak, and new Raman peaks appear at 998 cm<sup>-1</sup> and 1022 cm<sup>-1</sup> can be observed. This phenomenon can be attributed to the vibration of the S-O bond, indicating the formation of the sulfate species. The results show that the sulfur poisoning phenomenon of the catalyst can occur under high SO<sub>2</sub> concentration, which can be attributed to the fact that some SO<sub>2</sub> is oxidized to SO<sub>3</sub> and combined with the active components to form sulfate species [57,76]. However, due to the concentration of SO<sub>2</sub> in diesel exhaust is only a few ppm, and with the future development, the purification of diesel will further reduce the concentration of sulfur in exhaust. Therefore, the K<sub>0.15</sub>Mn<sub>0.5</sub>Ce<sub>0.5</sub>O<sub>8</sub> catalyst has high potential in future CDPF applications.

In addition to SO<sub>2</sub> in diesel engine exhausts, the presence of water vapor also has a certain impact on soot combustion. Therefore, it is also significant to investigate the effect of SO<sub>2</sub> on catalysts in the presence of water vapor. In this study, the effects of 0 ppm, 10 ppm, 100 ppm, and 300 ppm SO<sub>2</sub> on the K<sub>0.15</sub>Mn<sub>0.5</sub>Ce<sub>0.5</sub>O<sub>8</sub> catalyst were investigated under 10% H<sub>2</sub>O atmosphere (Fig. 9F). In the presence of 10% H<sub>2</sub>O in the

reaction atmosphere, the catalysts exhibited better catalytic activity than without H<sub>2</sub>O, which may be related to the formation of protonated substances (such as HNO<sub>3</sub>) or a decrease in activation energy [80,81]. Interestingly, this promotion effect was also observed for coexisting water vapor and SO<sub>2</sub>. The catalytic activity of the K<sub>0.15</sub>Mn<sub>0.5</sub>Ce<sub>0.5</sub>O<sub>8</sub> catalyst in 10% H<sub>2</sub>O, 10 ppm SO<sub>2</sub> and 10% H<sub>2</sub>O, and 100 ppm SO<sub>2</sub> did not decrease significantly compared with that under a sulfur-free and anhydrous atmosphere. When the concentration of SO<sub>2</sub> increased to 300 ppm, the catalytic activity of K<sub>0.15</sub>Mn<sub>0.5</sub>Ce<sub>0.5</sub>O<sub>8</sub> decreased significantly, especially its T<sub>90</sub> activity. In addition, due to the loss of alkali metals under water-containing conditions, the activity of the catalyst may be reduced. Therefore, in order to further investigate the water resistance of the catalyst, the as-prepared catalysts were treated under water with different conditions, including soak in water for 12 h, heat treatment in water vapor at 100 °C and 500 °C for 12 h. The activity results are shown in Fig. 9G and Table S3, compared with fresh catalyst, the T<sub>10</sub> temperature of the treated catalysts is basically unchanged. In contrast, the catalytic activities of the treated catalysts by water have slight decline in temperature of T<sub>50</sub> and T<sub>90</sub>. However, the increased temperature of T<sub>50</sub> and T<sub>90</sub> is lower than 10 °C, which indicated that the water treatment exhibited low influence on the catalytic activity. As shown in the Fig. 9H, compared with the fresh catalyst, it can be concluded that the XRD diffraction peaks of the treated catalysts has well maintained except for the peak of 2θ=12.7°. Therefore, it can be obtained that K<sub>0.15</sub>Mn<sub>0.5</sub>Ce<sub>0.5</sub>O<sub>8</sub> catalyst exhibit certain water resistance. The certain water resistance can be largely attributed to the fact that the microscopic tunnel structure of cryptomelane K<sub>2-x</sub>Mn<sub>8</sub>O<sub>16</sub> has good limiting effect for K<sup>+</sup> ions, which is also ensured the stability of the crystal structure and performance of the catalyst.

### 3.3. Possible reaction mechanism of soot combustion on the As-prepared catalysts

The XRD results in Fig. 2 confirm that the K<sub>0.15</sub>Mn<sub>0.5</sub>Ce<sub>0.5</sub>O<sub>8</sub> catalyst comprises CeO<sub>2</sub> and cryptomelane K<sub>2-x</sub>Mn<sub>8</sub>O<sub>16</sub> (KMnO) crystal phases. Thus, in the DFT calculations, three computational models were considered, namely, CeO<sub>2</sub>, KMnO, and a CeO<sub>2</sub>/KMnO interface. The calculated lattice parameter for the CeO<sub>2</sub> unit cell was 5.437 Å, which well matches the experimentally measured value (5.412 Å). [82] The calculated lattice parameters of the KMnO unit cell were a = b = 9.776 Å, and c = 2.915 Å, which match the experimental values (a = b =

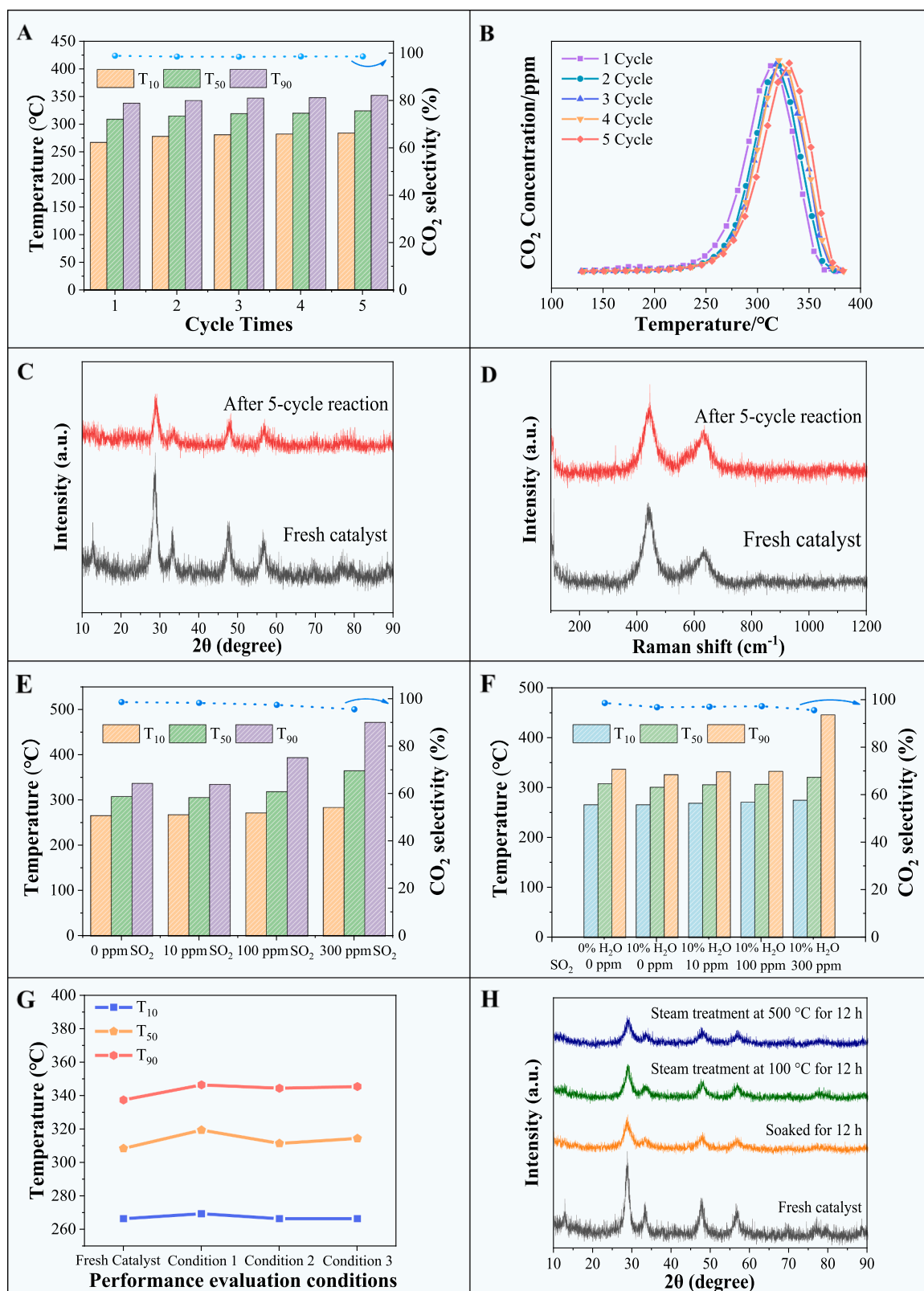


**Fig. 9.** K<sub>0.15</sub>Mn<sub>0.5</sub>Ce<sub>0.5</sub>O<sub>6</sub> Catalyst stability (A), CO<sub>2</sub> concentration curve of catalytic combustion of soot (B), XRD patterns (C), Raman spectra (D), Tolerance of sulfur dioxide (E), Tolerance of sulfur dioxide and water (F), Catalyst activity after water treatment - Condition 1: soak in water for 12 h; Condition 2: heat treatment in water vapor at 100 °C for 12 h; Condition 3: heat treatment in water vapor at 500 °C for 12 h (G), XPD patterns of catalyst after water treatment (H).



**Table 2**  
catalytic activity of as-prepared catalysts for soot combustion.

Catalysts	T <sub>10</sub> /°C	T <sub>50</sub> /°C	T <sub>90</sub> /°C	SCO <sub>2</sub> <sup>o</sup> /%
MnO <sub>8</sub>	315	380	420	97.9%
CeO <sub>6</sub>	330	392	432	85.7%
MnCeO <sub>8</sub>	282	344	381	99.7%
K <sub>0.3</sub> MnO <sub>8</sub>	274	324	352	98.4%
K <sub>0.03</sub> Mn <sub>0.1</sub> Ce <sub>0.9</sub> O <sub>8</sub>	280	323	348	99.5%
K <sub>0.09</sub> Mn <sub>0.3</sub> Ce <sub>0.7</sub> O <sub>8</sub>	279	318	348	98.5%
K <sub>0.15</sub> Mn <sub>0.5</sub> Ce <sub>0.5</sub> O <sub>8</sub>	267	309	338	98.9%
K <sub>0.21</sub> Mn <sub>0.7</sub> Ce <sub>0.3</sub> O <sub>8</sub>	271	319	350	98.6%
K <sub>0.27</sub> Mn <sub>0.9</sub> Ce <sub>0.1</sub> O <sub>8</sub>	281	329	358	98.4%

9.766 Å, and  $c = 2.842$  Å [83]. According to the HRTEM characterization results shown in Figs. 4k and 4l, a CeO<sub>2</sub>(111) surface with a 4 × 3 supercell and a KMnO(112) surface with a 2 × 2 supercell were employed to study the surface reactions. A vacuum gap of 15 Å in the z direction was used to separate the neighboring slabs. The CeO<sub>2</sub>/KMnO interface was modeled by adding a Ce<sub>8</sub>O<sub>16</sub> layer on the KMnO(112) surface. The optimized structural models of the CeO<sub>2</sub>(111) surface, KMnO(112) surface, and CeO<sub>2</sub>/KMnO interface are shown in Fig. 10 A.

The oxygen vacancy formation energy ( $E_{OV}$ ) can be used to evaluate the oxidation ability of surface lattice O in metal oxide catalysts. Thus, oxygen vacancy formation energies were calculated for the CeO<sub>2</sub>(111) surface, KMnO(112) surface, and CeO<sub>2</sub>/KMnO interface. As shown in Fig. 10B, the CeO<sub>2</sub>/KMnO interface shows a remarkably decreased  $E_{OV}$  of −1.19 eV, indicating that the activity of lattice O at the CeO<sub>2</sub>/KMnO interface is greatly promoted. This could be attributed to the fact that the strong interaction between CeO<sub>2</sub> and KMnO results in significant structure distortion at the interface of these two oxide phases and thus weakens the bonding strength of interfacial O. These DFT-calculated results are in agreement with the H<sub>2</sub>-TPR results shown in Fig. 5A, which show that the K<sub>0.15</sub>Mn<sub>0.5</sub>Ce<sub>0.5</sub>O<sub>8</sub> catalyst with mixed CeO<sub>2</sub> and

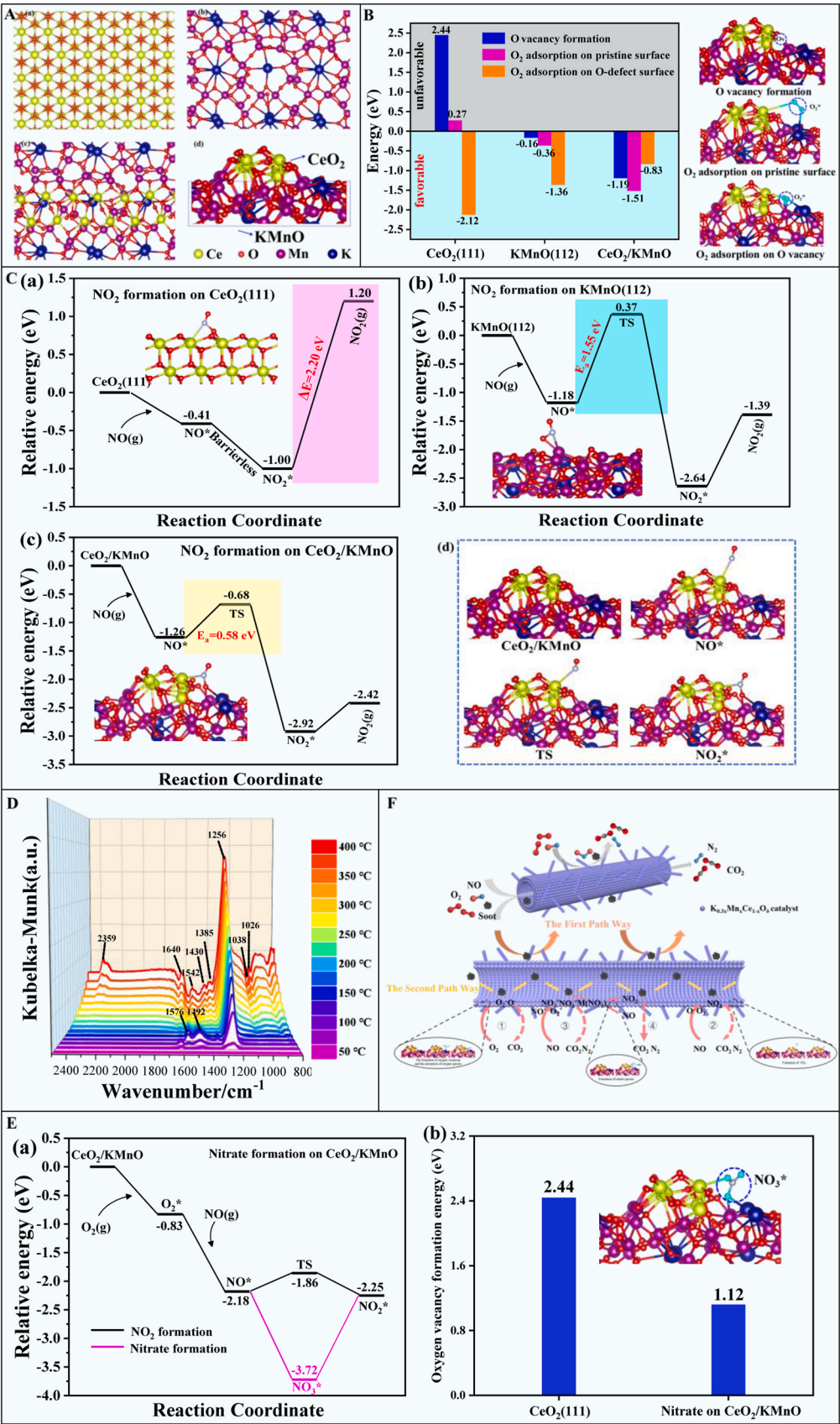
cryptomelane K<sub>2-x</sub>Mn<sub>8</sub>O<sub>16</sub> crystal phases exhibits a lower reduction temperature than the other catalysts with a single CeO<sub>2</sub> phase or KMnO structure, and is also consistent with the CO<sub>2</sub> concentration measured under anaerobic conditions in Fig. S3, indicating that the K<sub>0.15</sub>Mn<sub>0.5</sub>Ce<sub>0.5</sub>O<sub>8</sub> catalyst has the largest amount of active oxygen species.

Surface-adsorbed molecular O<sub>2</sub>\* could also be an active species in soot oxidation. Thus, the O<sub>2</sub> adsorption energy on the CeO<sub>2</sub>(111) surface, KMnO(112) surface, and CeO<sub>2</sub>/KMnO interface were also calculated, with the results shown in Fig. 10B. The results indicate that the CeO<sub>2</sub>/KMnO interface is favorable to the formation of active chemisorbed O<sub>2</sub>\* species on either a non-defective site ( $E_{ads} = -1.51$  eV) or O-defect site ( $E_{ads} = -0.83$  eV), while the O<sub>2</sub> adsorption on the non-defective sites of CeO<sub>2</sub> and KMnO is rather weak, with adsorption energies of 0.27 eV and −0.36 eV, respectively. These DFT-calculated results are consistent with XPS results shown in Table 1 and Fig. 7, which indicate that the K<sub>0.03</sub>Mn<sub>0.1</sub>Ce<sub>0.9</sub>O<sub>8</sub> catalyst comprising mixed CeO<sub>2</sub> and KMnO crystal phases contains more chemisorbed oxygen species compared to the other catalysts. Therefore, it can be concluded that the CeO<sub>2</sub>/KMnO interface achieves the co-activation of surface lattice oxygen and adsorbed molecular oxygen, which endows the K<sub>0.15</sub>Mn<sub>0.5</sub>Ce<sub>0.5</sub>O<sub>8</sub> catalyst comprising mixed CeO<sub>2</sub> and KMnO crystal phases with enhanced oxidation ability.

NO<sub>2</sub> has also been recognized as an important active oxidant that participates in soot combustion. Therefore, the oxidation of NO to NO<sub>2</sub> on the catalyst is also critical in the soot oxidation process. The detailed reaction processes for NO<sub>2</sub> formation on the CeO<sub>2</sub>(111) surface, KMnO(112) surface, and CeO<sub>2</sub>/KMnO interface were calculated, with the results shown in Fig. 10 C. The rate-limiting step for NO<sub>2</sub> formation on the CeO<sub>2</sub>(111) surface, which is the desorption of NO<sub>2</sub>\*, is largely hindered due to the high desorption energy barrier of 2.20 eV. This is in agreement with the calculated high oxygen vacancy formation energy of

**Table 3**  
Catalytic activities of as-prepared catalysts and reported catalysts for soot combustion.

Catalysts	soot/catalyst weight ratio	Contact mode	Reaction conditions	Heating rate (°C/min)	T <sub>10</sub> /T <sub>i</sub> (°C)	T <sub>50</sub> /T <sub>m</sub> (°C)	T <sub>90</sub> /T <sub>f</sub> (°C)	Ref
Ce-NC	1:9	loose	Flow 100 ml min <sup>−1</sup> , 50% N <sub>2</sub> +50% air	5	419	476	583	[63]
Ce <sub>0.5</sub> Pr <sub>0.5</sub> O <sub>2</sub>	1:4	loose	Flow 500 ml min <sup>−1</sup> , 5% O <sub>2</sub> +500 ppm NO+N <sub>2</sub> balance	10	371	444	511	[64]
Co/Ce-YSZ	1:4	loose	Flow 500 ml min <sup>−1</sup> , 5% O <sub>2</sub> +500 ppm NO+N <sub>2</sub> balance	-	392	509	605	[65]
Cu2CZ-Ti	1:4	loose	Flow 500 ml min <sup>−1</sup> , 5% O <sub>2</sub> +500 ppm NO+N <sub>2</sub> balance	10	425	505	583	[66]
Mn <sub>2</sub> O <sub>3</sub>	1:15	Tight	Flow 500 ml min <sup>−1</sup> , 15% O <sub>2</sub> +2% H <sub>2</sub> O+N <sub>2</sub> balance	3.3	301	356	397	[67]
Birnessite	1:4	loose	Flow 500 ml min <sup>−1</sup> , 5% O <sub>2</sub> +500 ppm NO+N <sub>2</sub> balance	10	379	453	530	[68]
Ce <sub>0.8</sub> K <sub>0.2</sub> CoO <sub>3</sub>	1:10	loose	Flow 200 ml min <sup>−1</sup> , 5% O <sub>2</sub> +1000 ppm NO+N <sub>2</sub> balance	2	326	383	426	[69]
Ce <sub>0.64</sub> Mn <sub>0.36</sub> real-2Mn1Ce	1:10	loose	Flow 500 ml min <sup>−1</sup> , 10% O <sub>2</sub> +Ar balance	5	278	-	433	[70]
	1:10	loose	Flow 50 ml min <sup>−1</sup> , 10% O <sub>2</sub> +10% H <sub>2</sub> O+500 ppm NO+Ar balance	-	395	466	510	[71]
CeMnO <sub>x</sub> -ES	1:10	Tight	Flow 100 ml min <sup>−1</sup> , 10% O <sub>2</sub> +250 ppm NO+N <sub>2</sub> balance	5	277	319	350	[72]
M10-CZ	1:10	loose	Flow 500 ml min <sup>−1</sup> , 0.5% O <sub>2</sub> +N <sub>2</sub> balance	5	-	520 ± 1	605 ± 1	[73]
Mn/CZ	1:10	loose	Flow 500 ml min <sup>−1</sup> , 10% O <sub>2</sub> +600 ppm NO+N <sub>2</sub> balance	-	381	531	-	[74]
CuMnO(K)	1:10	loose	Flow 200 ml min <sup>−1</sup> , 10% O <sub>2</sub> +500 ppm NO+N <sub>2</sub> balance	5	-	319	338	[75]
40% K-OMS-2/M-m TSO	1:10	loose	Flow 50 ml min <sup>−1</sup> , 10% O <sub>2</sub> +2000 ppm NO+Ar balance	2	295	345	377	[76]
KMnO <sub>x</sub> /M-m TSO-0.7	1:10	loose	Flow 50 ml min <sup>−1</sup> , 10% O <sub>2</sub> +2000 ppm NO+Ar balance	2	294	352	387	[77]
La <sub>0.8</sub> Ce <sub>0.1</sub> Co <sub>0.1</sub> MnO <sub>3</sub>	1:10	loose	Flow 50 ml min <sup>−1</sup> , 10% O <sub>2</sub> +2000 ppm NO+Ar balance	2	268	314	350	[78]
3DOM K <sub>0.5</sub> MnCeO <sub>x</sub> /SiO <sub>2</sub> -40	1:10	loose	Flow 50 ml min <sup>−1</sup> , 10% O <sub>2</sub> +2000 ppm NO+Ar balance	2	273	315	348	[79]
K <sub>0.15</sub> Mn <sub>0.5</sub> Ce <sub>0.5</sub> O <sub>8</sub>	1:10	loose	Flow 50 ml min <sup>−1</sup> , 10% O <sub>2</sub> +2000 ppm NO+Ar balance	2	267	309	338	This Work



(caption on next page)

**Fig. 10.** (A) Optimized structural models of (a) CeO<sub>2</sub>(111) surface, (b) KMnO(112) surface, (c) top view of CeO<sub>2</sub>/KMnO interface, and (d) side view of CeO<sub>2</sub>/KMnO interface. Yellow, red, purple, and blue balls represent Ce, O, Mn, and K atoms, respectively. These notations are used throughout this work. (B) Oxygen vacancy formation energies and molecular O<sub>2</sub> adsorption energies on CeO<sub>2</sub>(111) surface, KMnO(112) surface, and CeO<sub>2</sub>/KMnO interface. (C) Energy profiles for NO oxidation to form NO<sub>2</sub> on (a) CeO<sub>2</sub>(111) surface, (b) KMnO(112), and (c) CeO<sub>2</sub>/KMnO interface, and (d) corresponding optimized structures in the reaction pathway on CeO<sub>2</sub>/KMnO interface. (D) In situ DRIFTS spectra of K<sub>0.15</sub>Mn<sub>0.5</sub>Ce<sub>0.5</sub>O<sub>8</sub> catalyst. (E) (a) Energy profiles for nitrate species formation on CeO<sub>2</sub>/KMnO interface, and (b) oxygen vacancy formation energy of the nitrate species. (F) Reaction mechanism of K<sub>0.15</sub>Mn<sub>0.5</sub>Ce<sub>0.5</sub>O<sub>8</sub> catalysts for soot combustion.

2.44 eV on CeO<sub>2</sub>(111). As for the KMnO(112) surface, NO\* oxidation to NO<sub>2</sub>\* is the rate-limiting step and has a high energy barrier of 1.55 eV, and the desorption of NO<sub>2</sub>\* also has a relative high energy barrier of 1.25 eV. These results indicate that both the CeO<sub>2</sub>(111) and KMnO(112) surfaces are unfavorable for NO<sub>2</sub> formation. In comparison with CeO<sub>2</sub> and KMnO, the CeO<sub>2</sub>/KMnO interface not only has a lower energy barrier (0.58 eV) for NO oxidation to NO<sub>2</sub>\* but also has a lower desorption energy barrier (0.50 eV) for NO<sub>2</sub>\* desorption. Thus, it is suggested that the CeO<sub>2</sub>/KMnO interface substantially promotes the formation of the key active NO<sub>2</sub>\* species and thus benefits the NO<sub>x</sub>-assisted soot oxidation process. As shown in Fig. 8, these DFT-calculated results are in line with the experimental NO-TPO results, indicating that the NO oxidation ability of the CeO<sub>8</sub> catalyst is poor and that the K<sub>0.15</sub>Mn<sub>0.5</sub>Ce<sub>0.5</sub>O<sub>8</sub> catalyst with mixed CeO<sub>2</sub> and cryptomelane K<sub>2-x</sub>Mn<sub>8</sub>O<sub>16</sub> crystal phases exhibits lower reaction temperatures for NO oxidation and NO<sub>2</sub> formation than CeO<sub>8</sub> and KMnO.

In order to determine the type of NO<sub>x</sub> adsorbed on the surface of K<sub>0.15</sub>Mn<sub>0.5</sub>Ce<sub>0.5</sub>O<sub>8</sub> catalyst during soot combustion, the in-situ DRIFTS data of NO adsorption varying with temperature were recorded, with the results shown in Fig. 10D. The in-situ DRIFTS data were recorded under a feed gas of 2000 ppm NO, 10% O<sub>2</sub>, and Ar from 50 to 400 °C at 50 °C intervals. Most of the adsorbed species during the catalytic combustion of soot are the isomerization products of NO molecules, such as gas-phase CO<sub>2</sub> (2359 cm<sup>-1</sup>), gas-phase weakly-adsorbed NO<sub>2</sub> (1640 cm<sup>-1</sup>), chelated bidentate carbonate (1542 cm<sup>-1</sup>) [84], monodentate nitrate (1430 cm<sup>-1</sup>), ion nitrate (1385 cm<sup>-1</sup>), and bidentate nitrate (1038 cm<sup>-1</sup> and 1026 cm<sup>-1</sup>) [85]. In the low-temperature region (100–250 °C), there are absorption bands at 1576 cm<sup>-1</sup> and 1492 cm<sup>-1</sup>, corresponding to chelated bidentate nitrate and monodentate nitrate, respectively [86, 87]. With an increase in temperature, the intensity of the absorption band first increases and then decreases. The absorption band at 1256 cm<sup>-1</sup> corresponds to bridged bidentate nitrate, and the intensity of the absorption band increases with an increase in temperature, which is the main nitrate species on the surface of the K<sub>0.15</sub>Mn<sub>0.5</sub>Ce<sub>0.5</sub>O<sub>8</sub> catalyst [88]. Therefore, it is inferred that the bridging bidentate nitrate plays an important role in promoting the catalytic combustion of soot. To determine the role of the nitrate species, the formation, transformation, and reactivity of nitrate species on the CeO<sub>2</sub>/KMnO interface were calculated, with the results shown in Fig. 10E(a). After O<sub>2</sub> and NO are co-adsorbed at the CeO<sub>2</sub>/KMnO interface, two possible pathways can proceed. One involves the adsorbed NO\* reacting with an O atom in the adsorbed O<sub>2</sub>\* species to form NO<sub>2</sub>\*. The other involves the combination of NO\* with O<sub>2</sub>\* to form a NO<sub>3</sub>\* species. It can be seen that the formation of NO<sub>3</sub>\* is much more favorable, which is exothermic by -1.54 eV. To evaluate the reactivity of the NO<sub>3</sub>\* species, the  $E_{Ov}$  of the NO<sub>3</sub>\* species was calculated and compared with that of CeO<sub>2</sub>, as shown in Fig. 10E(b). The  $E_{Ov}$  value of 1.12 eV for the NO<sub>3</sub>\* species is much lower than that of 2.44 eV for CeO<sub>2</sub>, indicating that the O in NO<sub>3</sub>\* is the active species. Considering that the reaction temperature for soot oxidation is as high as 300 °C, it is possible that the O in the NO<sub>3</sub>\* species participates in the oxidation of soot. In addition, it is also possible that the NO<sub>3</sub>\* species could decompose into NO<sub>2</sub> ( $\Delta E = 1.47$  eV) at a high temperature of ~300 °C, with NO<sub>2</sub> then oxidizing the soot.

Therefore, the above DFT-calculated results suggest that the interaction between CeO<sub>2</sub> and KMnO and the formation of a CeO<sub>2</sub>/KMnO interface have multi-functional effects on promoting catalytic soot oxidation, as shown in Fig. 10 F. On the one hand, the CeO<sub>2</sub>/KMnO interface benefits the formation of active surface lattice oxygen and

adsorbed molecular oxygen species, and thus soot can be readily oxidized by surface lattice O through the Mars-van Krevelen (MvK) mechanism or by adsorbed molecular oxygen species through the Langmuir-Hinshelwood mechanism. On the other hand, NO is easily oxidized to NO<sub>2</sub> and nitrate species at the CeO<sub>2</sub>/KMnO interface, which serve as active species to oxidize soot into CO<sub>2</sub>. All these factors conducive to the excellent catalytic performance of the K<sub>0.15</sub>Mn<sub>0.5</sub>Ce<sub>0.5</sub>O<sub>8</sub> catalyst comprising mixed CeO<sub>2</sub> crystal and cryptomelane K<sub>2-x</sub>Mn<sub>8</sub>O<sub>16</sub> crystal phases for soot combustion, as shown in Table 2.

Based on the above experimental results, the reaction mechanism of K<sub>0.15</sub>Mn<sub>0.5</sub>Ce<sub>0.5</sub>O<sub>8</sub> catalyst in catalytic soot combustion is shown in Fig. 10 F. Based on the special hollow nanotube structure of the K<sub>0.15</sub>Mn<sub>0.5</sub>Ce<sub>0.5</sub>O<sub>8</sub> catalyst, a high number of active sites are effectively exposed. When the soot particles are mixed with the catalysts, the soot particles have two pathways via which to effectively make contact with the catalysts. One involves the soot making contact with the outer surface of the K<sub>0.15</sub>Mn<sub>0.5</sub>Ce<sub>0.5</sub>O<sub>8</sub> nanotube catalyst under the action of reaction gas flow. The uniformly distributed nanoneedle structure on the surface of the nanotube will “intercept and resident” the soot and greatly prolong the effective residence time of the soot on the outer surface of the catalysts. Second, the diameter of the K<sub>0.15</sub>Mn<sub>0.5</sub>Ce<sub>0.5</sub>O<sub>8</sub> nanotube catalysts is much larger than that of soot, so a small amount of soot particles can penetrate deep into the interior of the catalyst and come into contact with the inner surface of the catalyst. Driven by the reaction gas flow, the soot particles exhibit a Brownian-like motion in the nanotube and collide repeatedly with the inner surface of the catalysts, which greatly improves the contact efficiency of the reaction. In summary, the hollow nanotube structure with uniformly distributed nanoneedles on its surface, when used in soot combustion, can effectively improve the transport capacity of soot and provide more contact opportunities between the catalysts and the soot particles.

The research works of Moulijn's group in 1998 demonstrated that under the condition of tight contact between catalyst and soot, the contribution of surface oxygen and lattice oxygen of metal oxide catalysts to the oxidation mechanism was very important [89]. Based on this work, the hierarchical hollow fiber structure of catalyst leads to the actual contact state of catalyst and soot being close to the tight contact mode. Therefore, soot is oxidized by adsorbed molecular oxygen species and surface lattice oxygen through the MvK mechanism were proposed as one of the reaction pathways for soot combustion. In addition, due to the high concentration of NO in the reaction gas of the activity evaluation reaction in this work, in the catalytic reaction process, the active oxygen species will preferentially combine with the NO\* adsorbed on the catalyst surface to generate NO<sub>2</sub> and nitrate species with strong oxidation ability, which promotes the combustion of soot and plays a leading role in the catalytic combustion of soot. As shown in Fig. 10 F, the soot catalytic combustion reaction mainly involves the following four reaction pathways. In the first reaction path, since the strong interaction between CeO<sub>2</sub> and KMnO weakens the bonding strength of the interfacial O, it is easier to produce more oxygen vacancies. In the meantime the adsorption energy of the CeO<sub>2</sub>/KMnO interface at the non-defective or O-defect site is lower, which is more beneficial to the adsorption of oxygen. Therefore, the K<sub>0.15</sub>Mn<sub>0.5</sub>Ce<sub>0.5</sub>O<sub>8</sub> catalyst can activate the surface lattice oxygen and adsorbed molecular oxygen into active oxygen species (O<sub>2</sub> and O\*), which can directly oxidize soot to CO<sub>2</sub> (denoted as ①). In the second reaction pathway, as the CeO<sub>2</sub>/KMnO interface not only has a low energy barrier for NO oxidation to NO<sub>2</sub>\* but



also has a low desorption energy for  $\text{NO}_2^*$  desorption, NO can be easily oxidized to strongly oxidizing  $\text{NO}_2$  by the  $\text{K}_{0.15}\text{Mn}_{0.5}\text{Ce}_{0.5}\text{O}_8$  catalyst.  $\text{NO}_2$  then directly oxidizes the soot (denoted as ②). In the third reaction pathway, after the co-adsorption of  $\text{O}_2$  and NO at the  $\text{CeO}_2/\text{KMnO}$  interface,  $\text{NO}^*$  combines with  $\text{O}_2^*$  to form bridging bidentate nitrate, chelating bidentate nitrate, and monodentate nitrate species. The strong oxidizing nitrate species then directly oxidize soot to produce  $\text{N}_2$  and  $\text{CO}_2$  (denoted as ③). Finally, in the fourth reaction pathway, these nitrate species are decomposed into  $\text{NO}_x$  during heating, and then the soot is oxidized (denoted as ④). Compared with the continuous regeneration trap (CRT) technology, NO needs to be oxidized to strong oxidizing  $\text{NO}_2$  by the noble metal catalysts supported by a flow-through monolith, and then the generated  $\text{NO}_2$  is used to oxidize the downstream soot particles to reduce the temperature of eliminating soot particles [90,91]. In this work, due to the excellent conversion ability for oxidization of NO to  $\text{NO}_2$  for  $\text{K}_{0.15}\text{Mn}_{0.5}\text{Ce}_{0.5}\text{O}_8$  catalyst, the most of NO was also firstly oxidized on the surface of catalysts and then released to surface of soot particles, finally the soot particles were oxidized by  $\text{NO}_2$ . Over the entire process of reaction catalysis, the  $\text{CeO}_2$  in the  $\text{K}_{0.15}\text{Mn}_{0.5}\text{Ce}_{0.5}\text{O}_8$  catalyst uses its unique oxygen storage and release capacity as a “support pool” to ensure the supply of  $\text{O}_2$ , and the excellent redox properties of  $\text{K}_{2-x}\text{Mn}_8\text{O}_{16}$  effectively promote the valence state cycling of  $\text{Ce}^{4+} \leftrightarrow \text{Ce}^{3+}$ ,  $\text{Mn}^{4+} \leftrightarrow \text{Mn}^{3+}$ , and  $\text{Mn}^{3+} \leftrightarrow \text{Mn}^{2+}$ , and then produces more active oxygen species. The synergistic effect of the two effectively enhances the intrinsic activity of the catalyst and makes the catalytic system very active at low temperatures.

#### 4. Conclusion

A series of nanofibrous  $\text{K}_{0.3x}\text{Mn}_x\text{Ce}_{1-x}\text{O}_8$  catalysts for the catalytic combustion of soot particles were prepared via centrifugal spinning for the first time, and the physicochemical properties of the catalysts were investigated by XRD, SEM, TEM,  $\text{H}_2$ -TPR,  $\text{O}_2$ -TPD, XPS, and other characterization methods. Among the catalysts,  $\text{K}_{0.15}\text{Mn}_{0.5}\text{Ce}_{0.5}\text{O}_8$  showed the best catalytic performance, with  $T_{10}$ ,  $T_{50}$ ,  $T_{90}$ , and  $S_{\text{CO}_2}^m/\%$  values of 267 °C, 309 °C, 338 °C, and 98.9%, respectively. The excellent catalytic activity of  $\text{K}_{0.15}\text{Mn}_{0.5}\text{Ce}_{0.5}\text{O}_8$  can be attributed to structural effects arising from its hollow nanotube structure with a uniform distribution of nanoneedles on its surface, and the improvement in its intrinsic activity as a result of the synergistic effects between  $\text{CeO}_2$  and  $\text{K}_{2-x}\text{Mn}_8\text{O}_{16}$ . In addition, the hollow fiber structure  $\text{K}_{0.3x}\text{Mn}_x\text{Ce}_{1-x}\text{O}_8$  catalysts prepared by centrifugal spinning method can be realized large-scale production through improvement of the technique and equipment, and then the produced catalysts can be coated on the DPF by the conventional coating method for industrialization. In addition, the as-prepared catalysts can be directly grown on the surface of DPF to achieve application through further improvement of experimental conditions and methods in the further. In summary, the fibrous  $\text{K}_{0.15}\text{Mn}_{0.5}\text{Ce}_{0.5}\text{O}_8$  catalyst with high activity, good stability, good sulfur and water resistance has great application prospects.

#### CRedit authorship contribution statement

**Siyu Gao:** Methodology, Investigation, Formal analysis, Data curation. **Chunlei Zhang:** Writing – original draft, Methodology, Investigation, Formal analysis, Data curation. **Shengran Zhou:** Visualization, Investigation, Formal analysis, Data curation. **Lanyi Wang:** Software, Investigation, Formal analysis. **Di Yu:** Visualization, Investigation, Formal analysis, Data curation. **Xuehua Yu:** Writing – review & editing, Project administration, Methodology, Investigation, Funding acquisition, Formal analysis, Data curation. **Xiaoqiang Fan:** Visualization, Software, Investigation, Formal analysis, Data curation. **Zhen Zhao:** Writing – review & editing, Validation, Supervision, Resources, Project administration, Funding acquisition, Conceptualization. **Bing Liu:** Writing – original draft, Visualization, Software, Data curation.

#### Declaration of Competing Interest

The authors declare that they have no known competing financial interests or personal relationships that could have appeared to influence the work reported in this paper.

#### Data Availability

No data was used for the research described in the article.

#### Acknowledgements

This work was supported by National Natural Science Foundation of China (22072095, 22372107, U1908204, 22202058); National Key Research and Development Program of China (2022YFB3506200, 2022YFB3504100); Excellent Youth Science Foundation of Liaoning Province (2022-YQ-20); Shenyang Science and Technology Planning Project (22-322-3-28); Liaoning Xingliao Talented Youth Top Talent Program (XLYC2203007); University Joint Education Project for China-Central and Eastern European Countries (2021097).

#### Appendix A. Supporting information

Supplementary data associated with this article can be found in the online version at doi:10.1016/j.apcatb.2024.124169.

#### References

- [1] P.A. Neeft, M. Makkee, J.A. Moulijn, Metal oxides as catalysts for the oxidation of soot, *Chem. Eng. J.* 64 (1996) 295–302.
- [2] Yu, C. Peng, Y. Ren, L.Y. Wang, C.L. Zhang, X.Q. Fan, X.H. Yu, Z. Zhao, Low temperature oxidation of diesel soot particles over one-dimensional  $2 \times 3$  tunnel-structured  $\text{Na}_2\text{Mn}_5\text{O}_{10}$  catalysts, *Appl. Catal. B: Environ.* 344 (2024) 123614.
- [3] C. Wei, P. Zhang, J. Xiong, Q. Yu, Q.Q. Wu, Z. Zhao, J. Liu,  $\text{SiO}_2$ -tolerant catalytic removal of soot particles over 3D ordered macroporous  $\text{Al}_2\text{O}_3$ -supported binary Pt–Co oxide catalysts, *Environ. Sci. Technol.* 54 (2020) 6947–6956.
- [4] Yu, L.Y. Wang, C.L. Zhang, C. Peng, X.H. Yu, X.Q. Fan, B. Liu, K.X. Li, Z.G. Li, Y. C. Wei, J. Liu, Z. Zhao, Alkali metals and cerium-modified La–Co-based perovskite catalysts: facile synthesis, excellent catalytic performance, and reaction mechanisms for soot combustion, *ACS Catal.* 12 (2022) 15056–15075.
- [5] A.A.L. Van Setten, M. Makkee, J.A. Moulijn, Science and technology of catalytic diesel particulate filters, *Catal. Rev.* 43 (2001) 489–564.
- [6] L. Zhang, D. Yu, C. Peng, L.Y. Wang, X.H. Yu, Y.C. Wei, J. Liu, Z. Zhao, Research progress on preparation of 3DOM-based oxide catalysts and their catalytic performances for the combustion of diesel soot particles, *Appl. Catal. B: Environ.* 319 (2022) 121946.
- [7] X. Yang, D.Y. Zhao, Z.N. Gao, Y. Tian, T. Ding, J. Zhang, Z. Jiang, X.G. Li, Interface interaction induced oxygen activation of cactus-like  $\text{Co}_3\text{O}_4/\text{OMS}-2$  nanorod catalysts in situ grown on monolithic cordierite for diesel soot combustion, *Appl. Catal. B: Environ.* 286 (2021) 119932.
- [8] M. Wagloehner, S. Nitzner-Noski, Kureti, Oxidation of soot on manganese oxide catalysts, *Chem. Eng. J.* 259 (2015) 492–504.
- [9] Peng, D. Yu, L.Y. Wang, X.H. Yu, Zhen Zhao, Recent advances in the preparation and catalytic performance of Mn-based oxide catalysts with special morphologies for the removal of air pollutants, *J. Mater. Chem. A* 9 (2021) 12947.
- [10] Singer, C. Hahn, D.Q. Phan, T. Russwurm, M. Wensing, M. Koegl, L. Zigan, S. Kureti, Oxidation of soot in gasoline exhaust on  $\text{Mn}_2\text{O}_3$  catalyst, *Appl. Catal. A Gen.* 663 (2023) 119316.
- [11] A. Guillén-Hurtado, A. García-García, Bueno-López, Isotopic study of ceria-catalyzed soot oxidation in the presence of  $\text{NO}_x$ , *J. Catal.* 299 (2013) 181–187.
- [12] Piumetti, B.V.D. Linden B, M. Makkee, P. Miceli, D. Fino, N. Russo, S. Bensaid, Contact dynamics for a solid–solid reaction mediated by gas-phase oxygen: study on the soot oxidation over ceria-based catalysts, *Appl. Catal. B: Environ.* 199 (2016) 96–107.
- [13] Y. Gao, D. Yu, S.R. Zhou, C.L. Zhang, L.Y. Wang, X.Q. Fan, X.H. Yu, Z. Zhao, Construction of cerium-based oxide catalysts with abundant defects/vacancies and their application to catalytic elimination of air pollutants, *J. Mater. Chem. A* 11 (2023) 19210.
- [14] Yu, C. Peng, X.H. Yu, L.Y. Wang, K.X. Li, Z. Zhao, Z.G. Li, Facile preparation of amorphous  $\text{Ce}_m\text{Mn}_n\text{O}_x$  catalysts and their good catalytic performance for soot combustion, *Fuel* 307 (2022) 121803.
- [15] A. Sacco, J.P. Bortolozzi, V.G. Milt, E.E. Miró, E.D. Banús, One step citric acid-assisted synthesis of Mn–Ce mixed oxides and their application to diesel soot combustion, *Fuel* 322 (2022) 124201.
- [16] Schöneborn, T. Harmening, J. Giménez-Mañogil, J.C. Martínez-Munuera, A. García-García, Improved  $\text{NO}_x$  storage/release properties of ceria-based lean  $\text{NO}_x$  trap compositions with  $\text{MnO}_x$  modification, *Materials* 12 (2019) 2127.

- [17] Krishna, M. Makkee, Soot oxidation over  $\text{NO}_x$  storage catalysts: activity and deactivation, *Catal. Today* 114 (2006) 48–56.
- [18] Mul, J.P.A. Neeft, F. Kapteijn, M. Makkee, J.A. Moulijn, Soot oxidation catalyzed by a Cu/K/Mo/Cl catalyst: evaluation of the chemistry and performance of the catalyst, *Appl. Catal. B: Environ.* 6 (1995) 339–352.
- [19] L. Zhang, D. Yu, C. Peng, L.Y. Wang, X.Q. Fan, X.H. Yu, Z. Zhao, Preparation of K modified three-dimensionally ordered macroporous  $\text{MnCeO}_x/\text{Ti}_0.7\text{Si}_0.3\text{O}_2$  catalysts and their catalytic performance for soot, *Combust., Process.* 9 (2021) 1149.
- [20] H. Yu, Z. Zhao, Y.C. Wei, J. Liu, J.M. Li, A.J. Duan, G.Y. Jiang, Synthesis of K-doped three-dimensionally ordered macroporous  $\text{Mn}_{0.5}\text{Ce}_{0.5}\text{O}_8$  catalysts and their catalytic performance for soot oxidation, *Chin. J. Catal.* 36 (2015) 1957–1967.
- [21] L. Mei, J. Xiong, Y.C. Wei, Y.L. Zhang, P. Zhang, Q. Yu, Z. Zhao, J. Liu, High-efficient non-noble metal catalysts of 3D ordered macroporous perovskite-type  $\text{La}_2\text{NiB}'\text{O}_6$  for soot combustion: Insight into the synergistic effect of binary Ni and B' sites, *Appl. Catal. B: Environ.* 275 (2020) 119108.
- [22] Legutko, P. Stelmachowski, X.H. Yu, Z. Zhao, Z. Sojka, A. Kotarba, Catalytic soot combustion—general concepts and alkali promotion, *ACS Catal.* 13 (2023) 3395–3418.
- [23] J. Feng, Q.H. Liu, Y.J. Chen, P.F. Zhao, Q. Peng, K. Cao, R. Chen, M.Q. Shen, B. Shan, Macroporous  $\text{SmMn}_2\text{O}_5$  mullite for  $\text{NO}_x$ -assisted soot combustion, *Catal. Sci. Technol.* 7 (2017) 838–847.
- [24] Fang, N.J. Feng, L. Wang, J. Meng, G. Liu, P. Zhao, P.F. Gao, J. Ding, H. Wan, G. F. Guan, Fabrication of perovskite-type macro/mesoporous  $\text{La}_{1-x}\text{K}_x\text{FeO}_{3-\delta}$  nanotubes as an efficient catalyst for soot combustion, *Appl. Catal. B: Environ.* 236 (2018) 184–189.
- [25] Andana, M. Piumetti, S. Bensaid, N. Russo, D. Fino, R. Pirone, Nanostructured ceria—praseodymia catalysts for diesel soot combustion, *Appl. Catal. B: Environ.* 197 (2016) 125–134.
- [26] J. Feng, Z.J. Zhu, P. Zhao, L. Wang, H. Wan, G.F. Guan, Facile fabrication of trepang-like  $\text{CeO}_2/\text{MnO}_2$  nanocomposite with high catalytic activity for soot removal, *Appl. Surf. Sci.* 515 (2020) 146013.
- [27] Lee, J.I. Park, Y.G. Shul, H. Einaga, Y. Teraoka, Ag supported on electrospun macro-structure  $\text{CeO}_2$  fibrous mats for diesel soot oxidation, *Appl. Catal. B: Environ.* 174–175 (2015) 185–192.
- [28] Y. Liang, B.F. Jin, M. Li, X.X. Yuan, J. Wan, W. Liu, X.D. Wu, S. Liu, Highly reactive and thermally stable Ag/YSZ catalysts with macroporous fiber-like morphology for soot combustion, *Appl. Catal. B: Environ.* 294 (2021) 120271.
- [29] Fang, N.J. Feng, P. Zhao, H. Wan, G.F. Guan, Potassium promoted macro-mesoporous  $\text{Co}_3\text{O}_4\text{--La}_{0.88}\text{Sr}_{0.12}\text{CoO}_{3-\delta}$  nanotubes with large surface area: a high-performance catalyst for soot removal, *J. Colloid Interface Sci.* 582 (2021) 569–580.
- [30] Fang, N.J. Feng, P. Zhao, C. Chen, X. Li, J. Meng, G. Liu, L. Chen, H. Wan, G. F. Guan, In situ exsolution of Co/CoO<sub>x</sub> core-shell nanoparticles on double perovskite porous nanotubular webs: a synergistically active catalyst for soot efficient oxidation, *Chem. Eng. J.* 372 (2019) 752–764.
- [31] Fang, P. Zhao, N.J. Feng, H. Wan, G.F. Guan, Surface engineering on porous perovskite-type  $\text{La}_{0.6}\text{Sr}_{0.4}\text{CoO}_{3-\delta}$  nanotubes for an enhanced performance in diesel soot elimination, *J. Hazard. Mater.* 399 (2020) 123014.
- [32] R. Liu, L.L. Hou, G.C. Yue, H.K. Li, J.S. Zhang, J. Liu, B.B. Miao, N. Wang, J. Bai, Z. M. Cui, T.X. Liu, Y. Zhao, Progress of fabrication and applications of electrospun hierarchically porous nanofibers, *Adv. Fiber Mater.* 4 (2022) 604–630.
- [33] Zhang, Z.W. Ru, Y.J. Sun, M. Zhang, J.C. Wang, M.Z. Ge, H.C. Liu, S.S. Wu, C. Y. Cao, X.R. Ren, J. Mi, Y. Feng, Recent advances in applications for air pollutants purification and perspectives of electrospun nanofibers, *J. Clean. Prod.* 378 (2022) 134567.
- [34] Boningari, D.K. Pappas, P.G. Smirniotis, Metal oxide—confined interweaved titania nanotubes M/TNT (M = Mn Cu Ce Fe V Cr and Co) for the selective catalytic reduction of  $\text{NO}_x$  in the presence of excess oxygen, *J. Catal.* 365 (2018) 320–333.
- [35] P. Zhang, R.M. Li, M.J. Wang, Y.S. Li, Y.M. Tong, P.P. Yang, Y.J. Zhu, Two steps synthesis of  $\text{CeTiO}_x$  oxides nanotube catalyst: Enhanced activity resistance of  $\text{SO}_2$  and  $\text{H}_2\text{O}$  for low temperature  $\text{NH}_3$ -SCR of  $\text{NO}_x$ , *Appl. Catal. B: Environ.* 282 (2021) 119542.
- [36] Y. Vakhurshev, T.B. Boitsova,  $\text{TiO}_2$  and  $\text{TiO}_2/\text{Ag}$  nanofibers: template synthesis structure and photocatalytic properties, *J. Porous Mater.* 28 (2021) 1023–1030.
- [37] W. Ko, B.I. Lee, Y.J. Chung, C.B. Park, Carboxymethyl cellulose—templated synthesis of hierarchically structured metal oxides, *Green. Chem.* 17 (2015) 4167–4172.
- [38] Z. Wang, W.S. Xu, Z.X. Qin, X.M. Liu, S. Mintova, Low-temperature synthesis of  $\alpha$ -alumina nanosheets on microfibrillar-structured Al-fibers for Pd-catalyzed CO oxidative coupling to dimethyl oxalate, *Catal. Today* 354 (2020) 158–166.
- [39] T. Zhao, L. Zhang, D.X. Zhen, S. Yoo, Y. Ding, D.C. Chen, Y. Chen, Q.B. Zhang, B. Doyle, X.H. Xiong, M.L. Liu, A tailored double perovskite nanofiber catalyst enables ultrafast oxygen evolution, *Nat. Commun.* 8 (2017) 14586.
- [40] B. Chen, P.L. Wang, P. Fang, T.Y. Ren, Y. Liu, C.P. Cen, H.Q. Wang, Z.B. Wu, Tuning the property of Mn—Ce composite oxides by titanate nanotubes to improve the activity selectivity and  $\text{SO}_2/\text{H}_2\text{O}$  tolerance in middle temperature  $\text{NH}_3$ -SCR reaction, *Fuel Process. Technol.* 167 (2017) 221–228.
- [41] Xia, J.G. Ju, W. Xu, C.K. Ding, B.W. Cheng, Preparation and characterization of hollow  $\text{Fe}_2\text{O}_3$  ultra-fine fibers by centrifugal spinning, *Mater. Des.* 96 (2016) 439–445.
- [42] Hromádka, M. Motola, V. Čičmancová, R. Bulánek, J.M. Macak, Facile synthesis of  $\text{WO}_3$  fibers via centrifugal spinning as an efficient UV- and VIS-light-driven photocatalyst, *Ceram. Int.* 47 (2021) 35361–35365.
- [43] Akia, K.A. Mkhoyan, K. Lozano, Synthesis of multiwall  $\alpha$ - $\text{Fe}_2\text{O}_3$  hollow fibers via a centrifugal spinning technique, *Mater. Sci. Eng. C* 102 (2019) 552–557.
- [44] Kresse, J. Furthmüller, Efficient iterative schemes for ab initio total-energy calculations using a plane-wave basis set, *Phys. Rev. B* 54 (1996) 11169–11186.
- [45] Kresse, J. Furthmüller, Efficiency of ab-initio total energy calculation for metals and semiconductors using a plane-wave basis set, *Comput. Mater. Sci.* 6 (1996) 15–50.
- [46] L. Dudarev, G.A. Botton, S.Y. Savrasov, C.J. Humphreys, A.P. Sutton, Electron—energy—loss spectra and the structural stability of nickel oxide: an LSDA+U study, *Phys. Rev. B* 57 (1998) 1505–1509.
- [47] J. Grimme, S. Antony, H. Ehrlich, A. Krieg, Consistent and accurate ab initio parametrization of density functional dispersion correction (DFT-D) for the 94 elements H—Pu, *J. Chem. Phys.* 132 (2010) 154104.
- [48] E. Blöchl, Projector augmented-wave method, *Phys. Rev. B* 50 (1994) 17953–17979.
- [49] P. Perdew, K. Burke, M. Ernzerhof, Generalized gradient approximation made simple, *Phys. Rev. Lett.* 77 (1996) 3865–3868.
- [50] Henkelman, H. Jónsson, Improved tangent estimate in the nudged elastic band method for finding minimum energy paths and saddle points, *J. Chem. Phys.* 113 (2000) 9978–9985.
- [51] B.P. Henkelman, H. Uberuaga, A. Jónsson, Climbing image nudged elastic band method for finding saddle points and minimum energy paths, *J. Chem. Phys.* 113 (2000) 9901–9904.
- [52] C. Li, N. Yuan, J.S. Qian, B.C. Pan,  $\text{Mn}_2\text{O}_3$  as an electron shuttle between peroxy monosulfate and organic pollutants: the dominant role of surface reactive Mn(IV) species, *Environ. Sci. Technol.* 56 (2022) 4498–4506.
- [53] Zheng, W.Q. Liao, J.Q. Ding, F.X. Xu, A.P. Jia, W.X. Huang, Z.H. Zhang, Unveiling the key factors in determining the activity and selectivity of  $\text{CO}_2$  hydrogenation over Ni/CeO<sub>2</sub> Catalysts, *ACS Catal.* 12 (2022) 15451–15462.
- [54] Yu, Y. Ren, X.H. Yu, X.Q. Fan, L.Y. Wang, R.D. Wang, Z. Zhao, K. Cheng, Y.S. Chen, Z. Sojka, A. Kotarba, Y.C. Wei, J. Liu, Facile synthesis of birnessite-type  $\text{K}_2\text{Mn}_4\text{O}_8$  and cryptomelane-type  $\text{K}_{2-x}\text{Mn}_9\text{O}_{16}$  catalysts and their excellent catalytic performance for soot combustion with high resistance to  $\text{H}_2\text{O}$  and  $\text{SO}_2$ , *Appl. Catal. B: Environ.* 285 (2021) 119779.
- [55] Legutko, J. Gryboś, M. Fedyna, J. Janas, A. Wach, J. Szałachetko, A. Adamski, X. H. Yu, Z. Zhao, A. Kotarba, Z. Sojka, Soot combustion over niobium-doped cryptomelane (K—OMS—2) nanorods—redox state of manganese and the lattice strain control the catalysts performance, *Catalysts* 10 (2020) 1390.
- [56] L. Yang, X.Y. Wang, H.L. Wang, X.B. Li, Q. Li, Y.M. Wu, Y. Peng, Y.L. Ma, J.H. Li, Surface tailoring on  $\text{SrMnO}_3/\text{SmMn}_2\text{O}_5$  for boosting the performance in diesel oxidation catalyst, *Appl. Catal. B: Environ.* 320 (2023) 121993.
- [57] H. Yu, L.Y. Wang, M.Z. Chen, X.Q. Fan, Z. Zhao, K. Cheng, Y.S. Chen, Z. Sojka, J. C. Wei, J. Liu, Enhanced activity and sulfur resistance for soot combustion on three-dimensionally ordered macroporous—mesoporous  $\text{Mn}_x\text{Ce}_{1-x}\text{O}_8/\text{SiO}_2$  catalysts, *Appl. Catal. B: Environ.* 254 (2019) 246–259.
- [58] Yu, X.H. Yu, C.L. Zhang, L.Y. Wang, X.Q. Fan, Z. Zhao, Y.C. Wei, J. Liu, J. Gryboś, B. Leszczyński, A. Wach, D. Wierzbicki, A. Kotarba, Z. Sojka, Layered  $\text{Na}_2\text{Mn}_3\text{O}_7$  decorated by Cerium as the robust catalysts for efficient low temperature soot combustion, *Appl. Catal. B: Environ.* 338 (2023) 123022.
- [59] J. Zhao, L. Deng, J. Liu, Y.H. Li, J.X. Liu, Z.C. Duan, J. Xiong, Z. Zhao, Y.C. Wei, W. Y. Song, Y.Q. Sun, Roles of surface—active oxygen species on 3DOM cobalt-based spinel catalysts  $\text{M}_3\text{Co}_{3-x}\text{O}_4$  (M = Zn and Ni) for  $\text{NO}_x$ -assisted soot oxidation, *ACS Catal.* 9 (2019) 7548–7567.
- [60] Fang, P. Zhao, N.J. Feng, C. Chen, X. Li, G. Liu, H. Wan, G.F. Guan, Construction of a hollow structure in  $\text{La}_{0.9}\text{K}_{0.1}\text{CoO}_{3-\delta}$  nanofibers via grain size control by Sr substitution with an enhanced catalytic performance for soot removal, *Catal. Sci. Technol.* 9 (2019) 4938–4951.
- [61] H. Yu, J.M. Li, Y.C. Wei, Z. Zhao, J. Liu, B.F. Jin, A.J. Duan, G.Y. Jiang, Three-dimensionally ordered macroporous  $\text{Mn}_x\text{Ce}_{1-x}\text{O}_8$  and  $\text{Pt}/\text{Mn}_{0.5}\text{Ce}_{0.5}\text{O}_8$  catalysts: synthesis and catalytic performance for soot oxidation, *Ind. Eng. Chem. Res.* 53 (2014) 9653–9664.
- [62] J. Kong, S.N. Song, W.N. Zhao, Z.J. Yu, Z.W. Xiang, G.Y. Li, W.P. Zhang, T.C. An, Unraveling a trade-off between positive effect and poisoning mechanism of soot over low-dose PtCu/CeO<sub>2</sub> for simultaneously photothermocatalytic removal of VOCs and soot, *Appl. Catal. B: Environ.* 339 (2023) 123118.
- [63] Piumetti, B. Linden, M. Makkee, P. Miceli, D. Fino, N. Russo, S. Bensaid, Contact dynamics for a solid-solid reaction mediated by gas-phase oxygen: study on the soot oxidation over ceria-based catalysts, *Appl. Catal. B: Environ.* 199 (2016) 96–107.
- [64] Guillén-Hurtado, A. García-García, A. Bueno-López, Active oxygen by Ce-Pr mixed oxide nanoparticles outperform diesel soot combustion Pt catalysts, *Appl. Catal. B: Environ.* 174–175 (2015) 60–66.
- [65] P. Yeste, M.A. Cauqui, J. Giménez-Mañogil, J.C. Martínez-Munuera, M.A. Muñoz, A. García-García, Catalytic activity of Cu and Co supported on ceria-yttria-zirconia oxides for the diesel soot combustion reaction in the presence of  $\text{NO}_x$ , *Chem. Eng. J.* 380 (2020) 12237.
- [66] Giménez-Mañogil, A. García-García, Identifying the nature of the copper entities over ceria-based supports to promote diesel soot combustion: synergistic effects, *Appl. Catal. A: Gen.* 542 (2017) 226–239.
- [67] Singer, S. Kureti, Soot oxidation in diesel exhaust on manganese oxide catalyst prepared by flame spray pyrolysis, *Appl. Catal. B: Environ.* 272 (2020) 11896.
- [68] Atribak, A. Bueno-López, A. García-García, P. Navarro, D. Frías, M. Montes, Catalytic activity for soot combustion of birnessite and cryptomelane, *Appl. Catal. B: Environ.* 93 (2010) 267–273.
- [69] T. Wang, Z.T. Han, Y.B. Liu, C.Q. Gao, X.X. Pan, S. Zhou, The influence of partial substitution of Ce with K in  $\text{CeMO}_3$  (M = Mn, Fe, Co, Ni, Cu) perovskite catalysts on soot combustion performance, *J. Environ. Chem. Eng.* 11 (2023) 110850.

- [70] Zhu, Q. Wang, L. Lan, S.H. Chen, J.J. Zhang, Effect of surface manganese oxide species on soot catalytic combustion of Ce–Mn–O catalyst, *J. Rare Earths* 40 (2022) 1238–1246.
- [71] Y. Dai, Z.H. Li, C.C. Li, C.S. Zhang, F. Wang, P.P. Liu, H.N. Qiao, Revealing the effects of preparation methods over Ce–MnO<sub>x</sub> catalysts for soot combustion: physicochemical properties and catalytic performance, *J. Ind. Eng. Chem.* 121 (2023) 15–26.
- [72] X. Liao, P. Liu, J. Zhang, C. Wang, L.W. Chen, D.F. Yan, Q.M. Ren, X.L. Liang, M. L. Fu, S. Steven L, D.Q. Ye, Electrospun Ce–Mn oxide as an efficient catalyst for soot combustion: Ce–Mn synergy, soot-catalyst contact, and catalytic oxidation mechanism, *Chemosphere* 334 (2023) 138995.
- [73] Yao, J.S. He, X. Jiang, Y. Jiao, J.L. Wang, Y.Q. Chen, Factors determining gasoline soot abatement over CeO<sub>2</sub>–ZrO<sub>2</sub>–MnO<sub>x</sub> catalysts under low oxygen concentration condition, *J. Energy Inst.* 93 (2020) 774–783.
- [74] S. He, P. Yao, J. Qiu, H.L. Zhang, Y. Jiao, J.L. Wang, Y.Q. Chen, Enhancement effect of oxygen mobility over Ce<sub>0.5</sub>Zr<sub>0.5</sub>O<sub>2</sub> catalysts doped by multivalent metal oxides for soot combustion, *Fuel* 286 (2021) 119359.
- [75] Zhao, X.X. Zhou, W.M. Huang, L.Y. Pan, M. Wang, Q.R. Li, J.L. Shi, H.R. Chen, The effect of KNO<sub>3</sub> modification on the performance of Cu–Mn oxide catalyst for enhanced soot combustion, *Chem. Cat. Chem.* 10 (2018) 1455–1463.
- [76] H. Yu, Y. Ren, D. Yu, M.Z. Chen, L.Y. Wang, R.D. Wang, X.Q. Fan, Z. Zhao, K. Cheng, Y.S. Chen, J. Grybos, A. Kotarba, Z. Sojka, Y.C. Wei, J. Liu, Hierarchical porous K–OMS–2/3DOM–m Ti<sub>0.7</sub>Si<sub>0.3</sub>O<sub>2</sub> catalysts for soot combustion: easy preparation high catalytic activity and good resistance to H<sub>2</sub>O and SO<sub>2</sub>, *ACS Catal.* 11 (2021) 5554–5571.
- [77] Peng, D. Yu, C.L. Zhang, M.Z. Chen, L.Y. Wang, X.H. Yu, X.Q. Fan, Z. Zhao, K. Cheng, Y.S. Chen, Y.C. Wei, J. Liu, Alkali/alkaline–earth metal–modified MnO<sub>x</sub> supported on three–dimensionally ordered macroporous–mesoporous Ti<sub>x</sub>Si<sub>1–x</sub>O<sub>2</sub> catalysts: Preparation and catalytic performance for soot combustion, *J. Environ. Sci.* 125 (2023) 82–94.
- [78] H. Yu, D. Yu, L.Y. Wang, Y. Ren, M.Z. Chen, X.Q. Fan, Z. Zhao, Z. Sojka, A. Kotarba, Y.C. Wei, J. Liu, Ultralight and spongy La–Mn–based perovskite catalysts modified by alkali metals and Ce: facile synthesis and excellent catalytic performance for soot combustion, *Catal. Sci. Technol.* 13 (2023) 1208.
- [79] H. Yu, Z. Zhao, Y.C. Wei, L.L. Zhao, J. Liu, Three-dimensionally ordered macroporous K<sub>0.5</sub>MnCeO<sub>x</sub>/SiO<sub>2</sub> catalysts: facile preparation and worthwhile catalytic performances for soot combustion, *Catal. Sci. Technol.* 9 (2019) 1372–1386.
- [80] X. Zhu, S.C. Du, S.B. Wang, X.X. Lu, M.W. Zhang, B. Zhang, F.Y. Liu, W. Xiao, Y. B. Guo, J. Ding, Z.L. Zhang, P.X. Gao, PGM-free metal oxide nanoarray forests for water-promoted low-temperature soot oxidation, *Appl. Catal. B: Environ.* 341 (2024) 123336.
- [81] N. Yang, Y. Wang, H.L. Wang, Y.N. Zhang, Y. Peng, J.H. Li, Water accelerates and directly participates soot oxidation: An isotopic study, *Appl. Catal. B: Environ.* 302 (2022) 120837.
- [82] Filtzschew, K. Hofmann, C. Hess, Ceria and Its Defect Structure: New Insights from a Combined Spectroscopic Approach, *J. Phys. Chem. C* 120 (2016) 6694–6703.
- [83] L. Su, M.J. Chen, L. Gong, H. Yang, C. Chen, J. Wu, L. Luo, G. Yang, L.L. Long, Boost activation of peroxy monosulfate by iron doped K<sub>2–x</sub>MnO<sub>16</sub>: Mechanism and properties, *Chin. J. Chem. Eng.* 57 (2023) 89–97.
- [84] P. Wang, X.T. Yan, X.L. Bi, L.G. Wang, Z.L. Zhang, Z. Jiang, T.C. Xiao, A. Umar, Q. Wang, Lanthanum–promoted copper–based hydrotalcites derived mixed oxides for NO<sub>x</sub> adsorption soot combustion and simultaneous NO<sub>x</sub>–soot removal, *Mater. Res. Bull.* 52 (2014) 119–127.
- [85] Y. Gao, X.L. Tang, H.H. Yi, S.Z. Zhao, J.G. Wang, T. Gu, Improvement of activity selectivity and H<sub>2</sub>O&SO<sub>2</sub>–tolerance of micro–meso–porous CrMn<sub>2</sub>O<sub>4</sub> spinel catalyst for low–temperature NH<sub>3</sub>–SCR of NO<sub>x</sub>, *Appl. Surf. Sci.* 466 (2019) 411–424.
- [86] L. Zhang, Y.X. Zhang, Q.Y. Su, Z.P. Wang, Q. Li, X.Y. Gao, Determination of intermediates and mechanism for soot combustion with NO<sub>x</sub>/O<sub>2</sub> on potassium–supported Mg–Al hydrotalcite mixed oxides by In Situ FTIR, *Environ. Sci. Technol.* 44 (2010) 8254–8258.
- [87] Li, J.H. Li, Y. Peng, H.Z. Chang, T. Zhang, S. Zhao, W.Z. Si, J.M. Hao, Mechanism of Arsenic poisoning on SCR catalyst of CeW/Ti and its novel efficient regeneration method with hydrogen, *Appl. Catal. B: Environ.* 184 (2016) 246–257.
- [88] B. Tan, Y.C. Wei, Y.Q. Sun, J. Liu, Z. Zhao, W.Y. Song, J.M. Li, X. Zhang, Simultaneous removal of NO<sub>x</sub> and soot particulates from diesel engine exhaust by 3DOM Fe–Mn oxide catalysts, *J. Ind. Eng. Chem.* 63 (2018) 84–94.
- [89] Mul, F. Kapteijn, C. Doornkamp, J.A. Moulijn, Transition metal oxide catalyzed carbon black oxidation: a study with <sup>18</sup>O<sub>2</sub>, *J. Catal.* 179 (1998) 258–266.
- [90] Setiabudi, M. Makkee, J.A. Moulijn, An optimal NO<sub>x</sub> assisted abatement of diesel soot in an advanced catalytic filter design, *Appl. Catal. B: Environ.* 42 (2003) 35–45.
- [91] Crocoll, S. Kureti, W. Weisweiler, Mean field modeling of NO oxidation over Pt/Al<sub>2</sub>O<sub>3</sub> catalyst under oxygen-rich conditions, *J. Catal.* 229 (2005) 480–489.